The flow in weak turbulent hydraulic jumps

By IB A. SVENDSEN[1], J. VEERAMONY[2],
J. BAKUNIN[1] AND J. T. KIRBY[1]

[1] Center for Applied Coastal Research, Department of Civil and Environmental Engineering,
University of Delaware, Newark, DE 19716, USA

[2] Center for Ocean and Atmospheric Modeling, Building 1103, Room 249,
Stennis Space Center, MS 39529, USA

Velocity and surface measurements in three turbulent hydraulic jumps are analysed in detail. The velocity measurements were obtained in a hydraulic flume using laser-Doppler velocimetry and the surface measurements were obtained using capacitance wave gauges. The purpose is to extract information about the flow field and the stresses in the jumps and the geometrical extension of the recirculating region called the roller. To achieve this we first ensure that the overall continuity and momentum conservation for the flow is satisfied. This includes comparison with the classical results for hydraulic jumps. It is found that deviations from uniform-depth Reynolds-averaged velocities and hydrostatic pressure give small but important corrections to the conservation equations. Careful evaluation of the velocity measurements in conjunction with the continuity equation makes it possible to determine the lower limit of the recirculating roller region. Measurements of the Reynolds stresses are analysed, in particular in the roller region, and a simple model established that illustrates the mechanisms of the flow in the roller and predicts well the stresses along the lower limits of the roller. In combination with the analysis of the vorticity distribution, this leads to a qualitative description of the processes for the generation of vorticity. It suggests both similarities and differences from the hypothesis of the existence of a shear layer inside the jump. Similarity profiles are developed for the variation of stresses, vorticity, and eddy viscosity along the lower limit of the roller. Finally, the total angular momentum for the jumps is examined and compared to the analysis of Hornung, Willert & Turner (1995).

1. Introduction

Hydraulic jumps are among the most puzzling flow phenomena that occur in nature under steady, one-directional flow conditions. They are important as energy dissipators in connection with engineering structures in rivers. In addition, the flow in hydraulic jumps has many similarities with waves breaking both in deep water and in the surf zone on a beach – an aspect which has further increased the interest in the phenomenon. Over the years, many studies have been published of the various mechanisms active in hydraulic jumps. Nevertheless, there are still details such as the mechanisms behind the distribution of vorticity and the flow in the violently turbulent front of the jump (the so-called 'roller') that are not fully understood.

It has been difficult to obtain reliable measurements of the flow inside the jump, which, particularly in the turbulent front, usually includes strong entrainment of air bubbles. One of the pioneering studies by Rouse, Siao & Nagarathnam (1959)

bypassed this problem by conducting the measurements in a wind tunnel in which the free surface was replaced by a smooth wall with the shape of the mean water surface in a jump. Though this approach also removed the important effect of gravity and surface-penetrating turbulence, the study gave useful results and insights and its careful analysis of the measurements set the standards for many later investigations. Rouse *et al.* used the then novel technique of hot-wire anemometry. Later, improved versions of this experimental technique made it possible to obtain measurements in real jumps in water (see Resch & Leutheusser, 1972; Resch, Leutheusser & Coantic 1976).

Laser-Doppler velocimetry has also been used both in regular hydraulic jumps (Kirby, Bakunin & Huq 1995) and in the closely related problem of breaking waves trailing hydrofoils (Battjes & Sakai 1981). Finally, the technique of particle image velocimetry (PIV) was pioneered for waves breaking behind an airfoil by Duncan (1981) (who did not have the signal processing tools of today) and later used for the same problem by Lin & Rockwell (1995), and for the flow far downstream of a hydraulic jump by Hornung, Willert & Turner (1995). Dabiri & Gharib (1997) also uses the digital PIV technique to study viscocity and capillary dominated jumps.

Recent years have also seen increasingly realistic steps toward numerical modelling of the flow in hydraulic jumps. Madsen & Svendsen (1983) presented a four variable model of the jump based on an extended version of the nonlinear shallow-water equations. The model, which was extended to unsteady bores by Svendsen & Madsen (1984), used parameterized velocity profiles and a simplified $k - \epsilon$ turbulent closure to determine the shape of the free-surface variation and the velocity parameters inside the jump. A somewhat analogous approach but without a turbulence closure was used by McCorquodale & Kalifa (1983).

Lately, more sophisticated modelling techniques have been used which include two equation closure models to monitor the development of the turbulence and the volume of fluid method (VOF) to describe the flow. Examples are Long, Steffler & Rajaratnam (1991), Quingchao & Drewes (1994), and Bowles & Smith (1992), some of which address various special cases such as submerged jumps or capillary influenced circular jumps. Yeh (1991) discusses the mechanisms for generation of vorticity in bores and finds that a gradient in fluid density is required.

In a very simplified model, Hornung *et al.* (1995) recently analysed the angular momentum balance in an ordinary hydraulic jump. Of particular interest is the contribution to the angular momentum from the non-hydrostatic pressure.

The purpose of the present paper is to extract information about the basic hydrodynamics of the flow inside hydraulic jumps. This is obtained through analysis of the high-accuracy measurements obtained by Bakunin (1995) combined with theoretical modelling. In order to achieve this, we first verify that the measurements satisfy the equations for conservation of mass and momentum. Through this process we determine the (constant) volume flux of the jumps and the Froude number. A generalized version of the classical formula relating Froude number and depth ratio for the jump is derived and the effect that non-uniform velocity profiles and deviation of hydrostatic pressures have for the momentum balance is analysed.

Particular emphasis is given to the flow in the recirculating roller region at the turbulent front of the jump. A simplified model for the flow and stresses in the roller is developed, and information about the vorticity distribution in the jump is obtained. Comparison with the measured shear stresses at the lower edge of the roller suggests that the roller flow may be more complicated than suggested by the simplified estimates for those stresses presented by e.g. Deigaard & Fredsøe (1989).
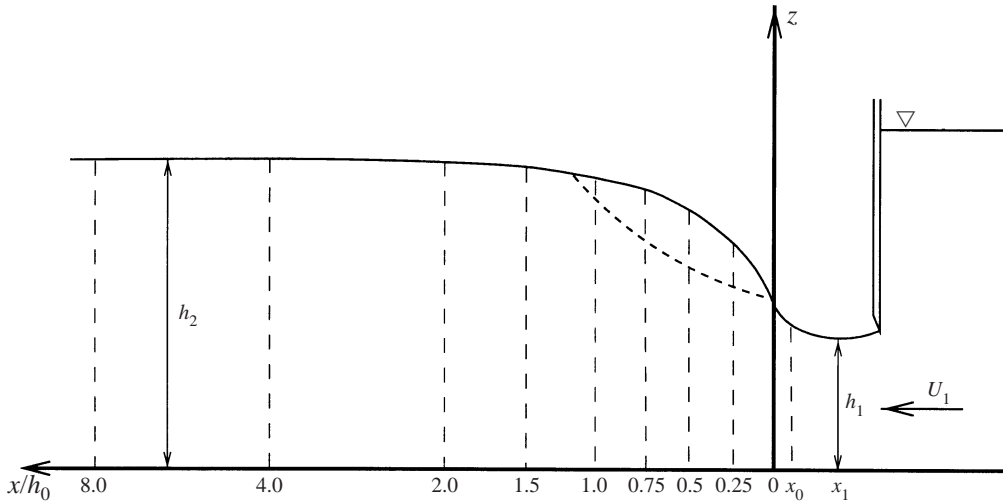
FIGURE 1. Sketch of experimental set-up and definition of parameters.

The somewhat puzzling issue of the angular momentum balance was raised in Hornung *et al.* (1995). We apply the experimental and theoretical results of this paper to analyse this in detail and it is found that because the basic assumptions of Hornung *et al.* are not satisfied, their conclusions must also be modified, in particular with respect to the need for a particular amount of (negative) vorticity downstream of the jump.

The paper is organized as follows. The experimental set-up for the measurements is briefly described in §2. Section 3 describes the initial analysis of the experimental results and establishment of the Froude number for the three jumps and §4 analyses the momentum balance in the jump. Both the overall and the local balance are discussed. In §5, the flow and stresses in the roller region are analysed and a simple model established particularly for the stresses at the lower edge of the roller. Section 6 gives the results for the vorticity in the jump and a discussion of the mechanisms for generation of vorticity, and in §7 the angular momentum balance is analysed. Further discussions and conclusions end the paper.

2. Description of the measurements

The measurements used in the present paper were reported by Bakunin (1995) and the experimental set-up is shown schematically in figure 1 which also shows the definition of the basic geometrical parameters for the jumps. In the following, the depth h_1 refers to the minimum depth in front of the jump where the depth-averaged velocity is U_1, h_0 is the measured depth at $x = x_0$ and h_2 is the depth sufficiently far downstream of the jump for the conditions to be largely uniform.

The jumps were generated downstream of an undershot weir in a closed circuit hydraulic flume by adjusting the discharge, the downstream overflow weir, and the height of the undershot weir. The inclination of the tank was set so that the downstream flow became uniform. The bottom of the tank was made of smooth steel and the walls of glass. The downstream overflow weir was positioned approximately 4.3 m (or 40 times h_2) downstream of the last measuring position at $x/h_0 = 8.0$.

Measurements were taken with a two-dimensional laser-Doppler velocimeter placed

Jump number	h_0 (m)	U_0 (m s^{-1})
1	0.072	0.9483
2	0.064	1.0597
3	0.059	1.1621

TABLE 1. Measured identification parameters for the jumps.

outside the glass walls and operated in back-scattering mode. The time variations of the horizontal (u) and vertical (w) velocities were obtained only along the centreline of the channel. The signal was processed using burst spectrum analysers, leading to an average data rate of 1000 Hz, which was subsequently bin-averaged to a 200 Hz rate.

The surface elevation was measured simultaneously by means of a capacitance wave gauge, sampled at 100 Hz. The diameter of the wire was 1 mm, which is believed to be small enough to make the surface disturbances generated around the wire by the wire itself negligible in comparison to the elevations in the jump. The vertical lines in figure 1 indicate verticals along each of which a large number of measurements were taken. In the following analysis, the origin of the horizontal x-axis is placed at the mean position of the toe of the turbulent front and the distances of the measuring sections from the toe are indicated in the figure. Further details of the experimental set-up may be found in Bakunin (1995). The mean position of the toe was determined by measuring the average distance of the toe from the measuring station at x_0.

Finally, it is mentioned that all measurements were taken along the centreline of the tank. Though no attempts were made to record the variations across the tank, visual observations indicate that the flow was uniform in the cross-channel direction. Thus, for symmetry reasons, lateral derivatives of the flow variables, including that of the intensity of the lateral turbulence fluctuation v', are therefore assumed small enough to be neglected.

Detailed measurements were performed for three different jumps. The measured identification parameters for the jumps (the depth h_0 at the only measuring section in the front of the jump, and the mean velocity U_0 at h_0) are given in table 1.

As will be seen in §3, the jumps correspond to relatively small values of the Froude number ($\mathcal{F} = 1.38, 1.46, 1.56$). These small values were chosen because they correspond to ratios between maximum and minimum depths in the jumps that are similar to the depth ratios between trough and crest for surf zone waves. Hence, such jumps provide the best similarity with nearshore breaking waves which was an important part of the motivation for the experiments. For completeness we notice that these values were large enough to make all the jumps turbulent. Only the smallest of the jumps showed a weak tendency of undular behaviour downstream of the turbulent front.

The scale of the experiments was also chosen to be small enough to minimize the entrainment of air bubbles at the turbulent front, which facilitated the LDV measurements and made it possible to measure well into the surface roller. As indicated by Banner & Phillips (1974) and later by Peregrine & Svendsen (1978) the generation of turbulence at the front of a hydraulic jump or breaking wave can occur without air entrainment. On the other hand, the jumps were large enough and the turbulence strong enough to render capillary forces negligible.

3. Volume flux and Froude number

The first goal is to ensure that the interpretation of measured velocities satisfies the conservation laws for mass and momentum throughout the jump. In order to achieve this, an analytical curve-fit is developed for the measured horizontal velocities along each of the verticals in the dataset. The verticals were divided into four sections and the following approximations used:

(*a*) The wall region: from the bottom ($z = 0$) to the first measurement location in the vertical, $z = z_1$ (~ 1 mm above the bottom), we used

$$u(z) = u_1 \left(\frac{z}{z_1} \right)^{1/7}. \tag{3.1}$$

(*b*) In the boundary layer $z_1 \leqslant z \leqslant \delta$, where δ is determined as the displacement thickness:

$$\delta = \int_0^h \left(1 - \frac{u}{U} \right) \mathrm{d}z, \tag{3.2}$$

we use the approximation

$$u = u_1 + C \log \left(\frac{z}{z_1} \right), \tag{3.3}$$

where C is found by a least-squares fit to the measured values in the boundary layer.

(*c*) A middle region for $\delta < z < z_2$, where the velocities are nearly constant. In this region, which constitutes the largest part of the depth, a fourth-order polynomial was used in a least-squares fit subject to continuity constraints in velocity and velocity gradients at the boundaries to regions (*b*) and (*d*).

(*d*) The upper region $z_2 < z < h$ includes the roller region. This is the region with the largest velocity variations and a third-order polynomial was used. As mentioned, the constraints in the least-squares fit were continuity in velocity and velocity gradient at the connection to region (*c*) and zero gradient at the mean free surface corresponding to zero (or small) shear stress there.

The original measurement values and the velocity profiles curve-fitted to the data as indicated are shown in figure 2. The measured position of the mean free surface (marked with a + is also shown). The lower limit of the roller, which is to be determined later, is marked with circles.

It can be seen that the curve-fitted profiles represent the measurements with high accuracy. In the following, this is further verified by using the measured velocities to determine the mean volume flux $\overline{Q}$ in the jump. The local (in x) value of the volume flux Q is defined as

$$Q = \int_{-B/2}^{B/2} \int_0^h u \, \mathrm{d}z \, \mathrm{d}y, \tag{3.4}$$

where B is the total width of the channel. No measurements of the lateral variation of the velocities were taken during the experiments, but it is found that the boundary layers along the glass sidewalls gave non-negligible reductions in the total volume flux. This effect was compensated for by assuming that the sidewall boundary layers are similar to the boundary layer along the bottom which was a smoothly painted steel wall. Hence, the integral over the cross-section in (3.4) was evaluated as

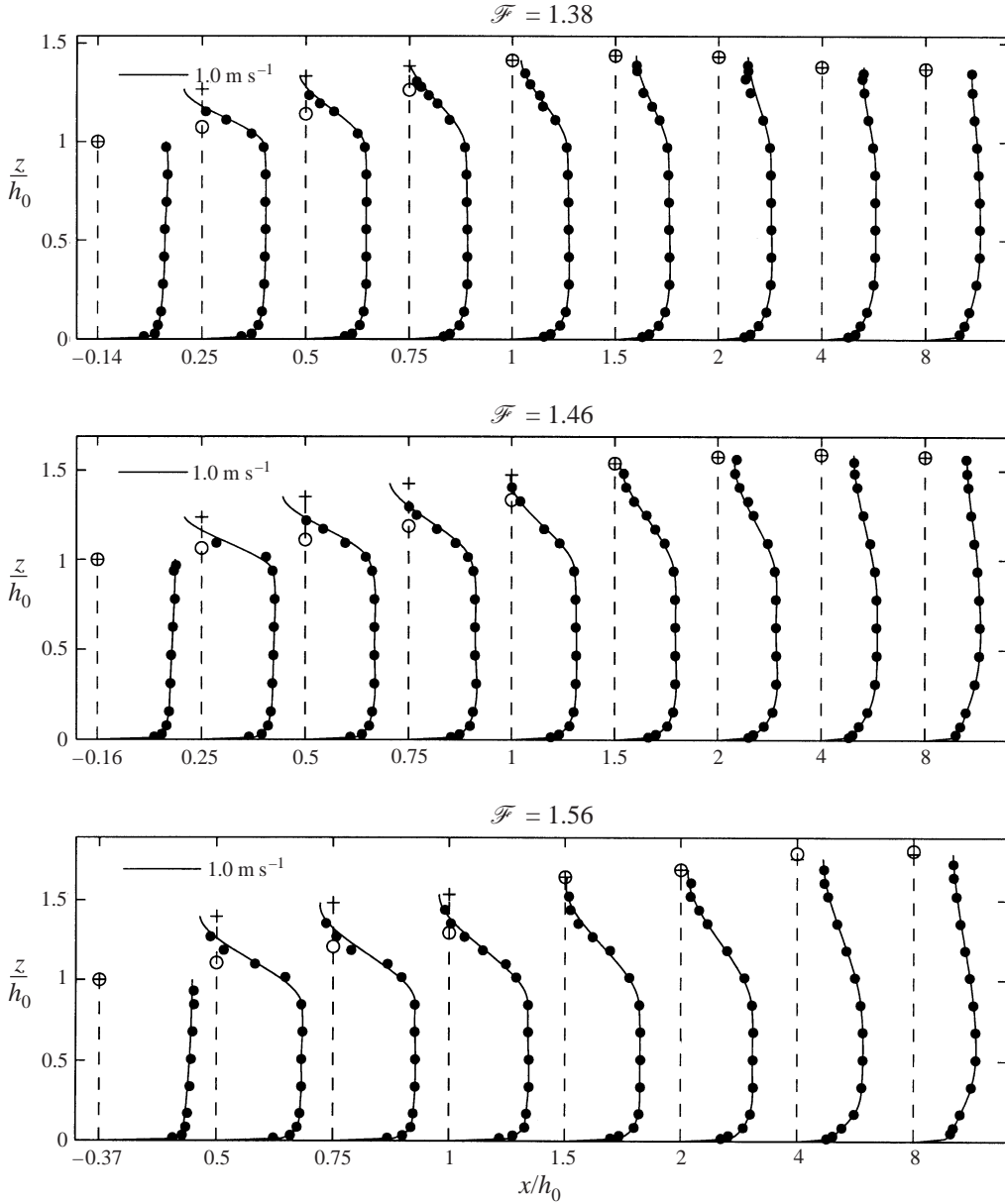$$Q = (B - 2\delta) \int_0^h u \, \mathrm{d}z, \tag{3.5}$$

FIGURE 2. $\bullet$, Measured horizontal velocities, and ——, curve-fits (solid line) versus z/h_0 for the values of x/h_0 where measurements were taken for all three jumps. $\circ$, The calculated lower limit of the dividing streamline; $+$, the measured mean water level at that location.

where δ was taken as the value determined from the vertical profiles. Figure 3 shows the variation of the total discharge in the three jumps found by this procedure. We see that for each jump the figure for the discharge stays within $\pm 0.05\%$ of a mean value. Knowing that Q is a constant, we therefore define the mean volume flux $\overline{Q}$ as
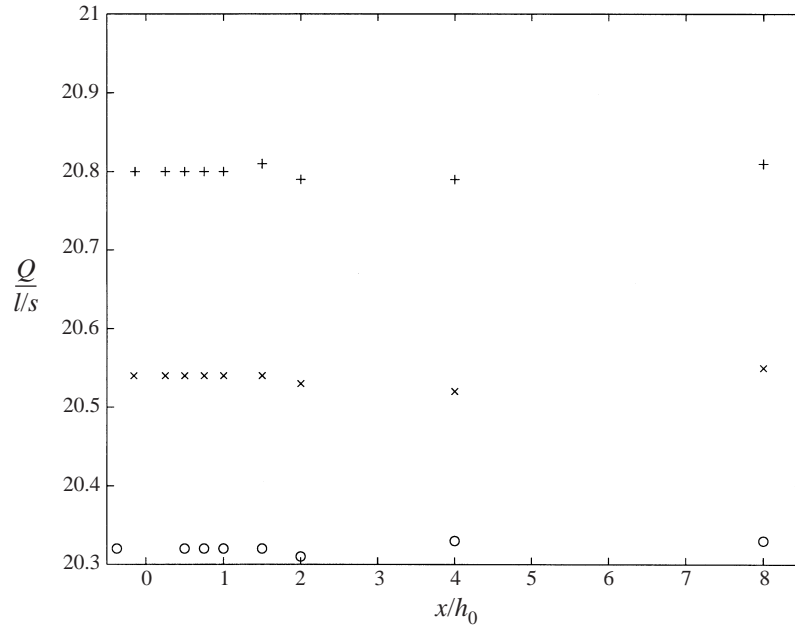
$$\overline{Q} = \frac{1}{L} \int_L Q \, dx, \tag{3.6}$$

FIGURE 3. Variation for computed volume fluxes $Q(x)$ for the values of x/h_0 where measurements were taken. $+$, $\mathscr{F} = 1.38$; $\times$, $\mathscr{F} = 1.46$; $\circ$, $\mathscr{F} = 1.56$.

where L is the length of the jump. In the following, that mean value is used as the discharge $\overline{Q}$ for each jump. These values are

$$\text{Jump number 1 } \overline{Q} = 20.80 \text{ l/s}$$
$$\text{Jump number 2 } \overline{Q} = 20.54 \text{ l/s}$$
$$\text{Jump number 3 } \overline{Q} = 20.32 \text{ l/s}$$

With $\overline{Q}$ known, it is possible to calculate the Froude number

$$\mathscr{F} = \frac{\overline{Q}}{A\sqrt{gh}} \tag{3.7}$$

for the jump, where $A = hB$. However, evaluation of $\mathscr{F}$ requires specification of h. In the experiments, the jumps were generated behind an undershot weir. The contraction of the cross-section at the weir created a weak depression of the water surface which resulted at a minimum water depth at some distance downstream of the weir (see figure 1). From this minimum position, the water surface again curved a little upward toward the toe of the jump, so that at the actual toe of the jump the surface had a non-zero slope. The measurements 'at the toe' were taken at distances of 10 mm, 10 mm and 22 mm, respectively, upstream of the mean position of the toe for jumps 1, 2 and 3, respectively. The water depth at that position was h_0. The slope on the mean water surface at this first measurement section can be judged by the values of the vertical mean velocities w at the point. They are shown in figure 4. We see that, even at the surface, the vertical velocity w at section x_0 is small in comparison to the horizontal velocity shown in figure 2.

Whereas the actual position where measurements were taken in front of the jump is somewhat arbitrary, the only well-defined depth in front of the jump is the minimum
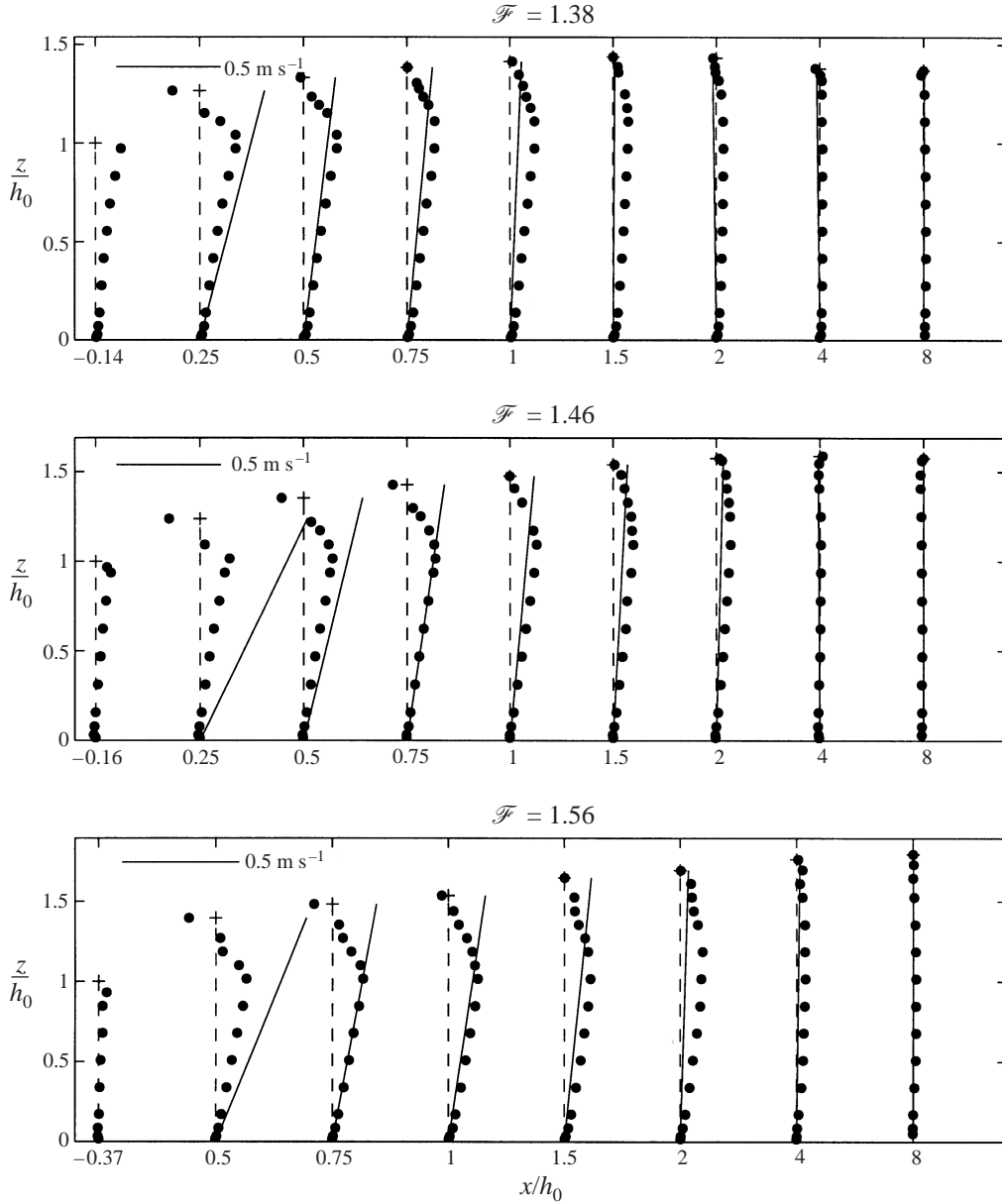
FIGURE 4. •, Measured values of the vertical velocities w versus z/h_0 for the values of x/h_0 where measurements were taken; ——, $w = U(\mathrm{d}h/\mathrm{d}x)$.

depth h_1 which occurs approximately midway between the weir and the toe. In the following, h_1 is used as the reference depth for each jump. As shown in §4, this makes it possible to determine the deviation from hydrostatic pressure in the front of the jump and the effect this has on the momentum balance. Unfortunately, the depth h_1 was not measured directly. It can be calculated, however, by assuming that between the weir and the toe the mean water surface can be approximated by a second-order Taylor expansion of the surface elevation around the minimum depth at x_1. Since

Jump number	h_0 (m)	u_s (m s^{-1})	w_s (m s^{-1})	R_s (m)	h_1 (m)	$\xi = \dfrac{h_2}{h_1}$	α_1	α_2	κ_1	κ_2
1	0.072	0.98	0.1275	1.087	0.063	1.565	1.0129	1.0194	1.063	1.00
2	0.064	1.12	0.08	2.437	0.060	1.680	1.0127	1.0260	1.037	1.00
3	0.059	1.19	0.04	5.894	0.057	1.889	1.0124	1.0360	1.017	1.00

TABLE 2. Values of $h_0, u_s\, w_s\, R_s,\, h_1, \xi, \alpha_1, \alpha_2, \kappa_1$ and κ_2.

$[\mathrm{d}h/\mathrm{d}x]_{x_1} = 0$ this expansion can be written as

$$h(x) = h(x_1) + \frac{(x - x_1)^2}{2R_s}, \tag{3.8}$$

where $R_s = [\mathrm{d}^2 h/\mathrm{d}x^2]^{-1}$ is the radius of curvature of the surface at x_1. Considering the relatively small correction ($1.7\% - 6.3\%$ in the momentum balance, see table 2) that the non-static pressure gives raise to, it is expected that this is a sufficiently accurate approximation. R_s and x_1 will be determined from the measurements at x_0 as follows.

The surface slope $\mathrm{d}h/\mathrm{d}x$ at the first measuring section x_0 is determined by differentiation of (3.8) which gives the value

$$\left(\frac{\mathrm{d}h}{\mathrm{d}x}\right)_{x_0} = \frac{x_0 - x_1}{R_s} \quad \text{at } x = x_0. \tag{3.9}$$

Since the free surface is a streamline, we also have

$$\left(\frac{\mathrm{d}h}{\mathrm{d}x}\right)_{x_0} = w_s/u_s. \tag{3.10}$$

Here, u_s and w_s denote the surface values of u and w. Then the radius of curvature R_s can be determined by combining (3.9) and (3.10) as

$$R_s = \frac{x_0 - x_1}{w_s/u_s}, \tag{3.11}$$

and we thus obtain

$$h_1 = h_0 - \tfrac{1}{2}(x_0 - x_1)\frac{w_s}{u_s}. \tag{3.12}$$

In calculating h_1, we have used a best fit for the measured values for u_s and w_s. The numbers used are shown in table 2. The values of h_0, R_s and h_1 are also shown.

Based on the values of $\overline{Q}$ and h_1, we obtain the values of $\mathscr{F}(\overline{Q})$ shown in table 3. The table also shows the Froude number $\mathscr{F}_0(\overline{Q})$ which is the only $\mathscr{F}$-value we can obtain by using the measured velocities and depth h_0 at x_0 directly. We see that the two $\mathscr{F}$-values differ substantially, especially for jump 1, which indicates the importance of the difference between h_0 and h_1.

4. Momentum balance in the jump

4.1. *Overall momentum balance*

Determination of the correct Froude number is also of interest in connection with the overall momentum balance in the jump, which gives the connection between the Froude number and the conjugate depth h_1 and depth h_2, the depth far downstream

Jump number	$\mathscr{F}$ ((3.7) with h_1)	$\mathscr{F}_0$ ((3.7) with h_0)	$\mathscr{F}'$ (4.1)	$\mathscr{F}$ (4.8)
1	1.378	1.128	1.416	1.371
2	1.464	1.326	1.500	1.472
3	1.562	1.484	1.652	1.621

TABLE 3. Measured and calculated Froude numbers for the jumps.

of the jump. In the classical theory, the assumptions of uniform-depth velocities and hydrostatic pressure at both h_1 and h_2 lead to the well-known expression

$$\mathscr{F}'^2 = \tfrac{1}{2}\xi(\xi + 1) \tag{4.1}$$

where $\xi \equiv h_2/h_1$. The results for $\mathscr{F}'$ determined from the calculated value of h_1 and h_2 measured at $x/h_0 = 8$ are also given in table 3. These values again differ from the value of $\mathscr{F}$ determined by (3.7). The reason is that the two basic assumptions behind (4.1) are not satisfied. The velocity u is not uniform over depth and the pressure is not hydrostatic, in particular not at x_1. To determine the correct expression for the momentum balance, we introduce the Reynolds decomposition

$$u = \widetilde{u} + u', \qquad \widetilde{u} = \frac{1}{T}\int_0^T u\,\mathrm{d}t, \tag{4.2}$$

$$w = \widetilde{w} + w', \qquad \widetilde{w} = \frac{1}{T}\int_0^T w\,\mathrm{d}t, \tag{4.3}$$

where T is the length of the time series. The momentum equation for constant density in the general form for a control volume covering vertical sections at h_1 and h_2 then becomes

$$\int_{A_1} (\rho(\widetilde{u}^2 + \widetilde{u'^2}) + p)\,\mathrm{d}A - \int_{A_2} (\rho(\widetilde{u}^2 + \widetilde{u'^2}) + p)\,\mathrm{d}A - \int_{x_1}^{x_2} (B + 2h)\tau_b\,\mathrm{d}x = 0 \tag{4.4}$$

where τ_b is the bottom friction. In the following, we will omit the $\widetilde{(\,)}$ over the ensemble averaged velocity except where ambiguous. We also assume that ρ is constant and again we assume that the sidewall friction is equal to the bottom friction.

Introducing momentum and pressure correction factors defined by

$$\alpha = \frac{A}{\overline{Q}^2}\int_A (u^2 + \widetilde{u'^2})\,\mathrm{d}A, \tag{4.5}$$

and

$$\kappa = \frac{2}{\rho g h^2 B}\int_A p\,\mathrm{d}A, \tag{4.6}$$

respectively, (4.4) can be written

$$\alpha_1 \frac{\overline{Q}^2}{g h_1^3 B^2} + \tfrac{1}{2}\kappa_1 = \alpha_2 \frac{\overline{Q}^2}{g h_1^3 B^2}\frac{1}{\xi} + \tfrac{1}{2}\kappa_2 \xi^2 + \tau', \tag{4.7}$$

where $\tau' \equiv (2/g B h_1^2)\int_{x_1}^{x_2}(B + 2h)\tau\,\mathrm{d}x$. Solving with respect to $\mathscr{F}^2 = \overline{Q}^2/g h_1^3 B^2$ then

gives

$$\mathscr{F}^2 = \tfrac{1}{2}\xi \frac{\kappa_2 \xi^2 - \kappa_1 + \tau'}{\alpha_1 \xi - \alpha_2}. \tag{4.8}$$

We notice here that setting α_1, α_2, κ_1, and $\kappa_2 = 1$ and $\tau' = 0$ reduces (4.8) to (4.1) as should be expected. Later, it will be shown that τ', the contribution from the bottom and sidewall friction, is negligible for the present measurements.

Evaluation of $\mathscr{F}$ from (4.8) requires determination of the α and κ coefficients. The α terms are determined directly from the definition (4.5) assuming the integration across the channel can be approximated by

$$\int_A (u^2 + \widetilde{u'^2})\,\mathrm{d}A \sim (B - 2\delta') \int_0^h (u^2 + \widetilde{u'^2})\,\mathrm{d}z, \tag{4.9}$$

where δ' is the momentum thickness determined for the vertical profiles and defined by

$$\delta' = \int_0^h \frac{u}{U}\left(1 - \frac{u}{U}\right)\mathrm{d}z \tag{4.10}$$

The curve-fitted velocities are used for the evaluation of (4.9) and the values are shown in table 2.

The pressure coefficient κ_1 is determined by realizing that

$$p(z) = \rho g(h - z) - \rho(w^2 + \widetilde{w'^2}) + \frac{\partial}{\partial x}\left[\int_z^h \rho(uw + \widetilde{u'w'})\mathrm{d}z\right]. \tag{4.11}$$

The measurements show that in (4.11) the contributions to p from the turbulent fluctuations are negligible. Figure 9 shows the values of $\widetilde{u'w'}$.

In order to determine $p(z)$ at x_1, we use the observation (figure 4) that at x_0 the vertical velocity w varies almost linearly from its zero value at the bottom to the value $u\mathrm{d}h/\mathrm{d}x$ at the surface. It is assumed that this applies to the entire region in front of the jump, and that for this calculation we can use the depth averaged value U of u, so that we can determine w from

$$\frac{w}{U} = \frac{z}{h}\frac{\mathrm{d}h}{\mathrm{d}x}. \tag{4.12}$$

In accordance with (3.8) we also have

$$\frac{\mathrm{d}h}{\mathrm{d}x} = \frac{x - x_1}{R_s}, \tag{4.13}$$

where R_s is given by (3.11). Introducing the dynamic pressure p_D defined by

$$p_D = p - \rho g(h - z), \tag{4.14}$$

and substituting (4.11) for p and (4.12) for w, we can write p_D as

$$p_D(z) = -\rho U^2 \frac{z^2}{h^2}\left(\frac{\mathrm{d}h}{\mathrm{d}x}\right)^2 + \frac{\mathrm{d}}{\mathrm{d}x}\left(\frac{1}{2h}\rho U^2(h^2 - z^2)\frac{\mathrm{d}h}{\mathrm{d}x}\right)$$

$$= -\rho U^2 \frac{z^2}{h^2}\left(\frac{\mathrm{d}h}{\mathrm{d}x}\right)^2 + \tfrac{1}{2}\rho \frac{\overline{Q}^2}{B^2}\frac{\mathrm{d}}{\mathrm{d}x}\left(\frac{h^2 - z^2}{h^3}\frac{\mathrm{d}h}{\mathrm{d}x}\right). \tag{4.15}$$

We then obtain, after some algebra

$$\int_0^h p_D(z)\,\mathrm{d}z = \tfrac{1}{3}\rho\frac{\overline{Q}^2}{B^2}h\frac{\mathrm{d}}{\mathrm{d}x}\left(\frac{1}{h}\frac{\mathrm{d}h}{\mathrm{d}x}\right), \tag{4.16}$$

and hence from (4.6)

$$\kappa = 1 + \tfrac{2}{3}\frac{\overline{Q}^2}{ghB^2}\frac{\mathrm{d}}{\mathrm{d}x}\left(\frac{1}{h}\frac{\mathrm{d}h}{\mathrm{d}x}\right). \tag{4.17}$$

At h_1 we have $\mathrm{d}h/\mathrm{d}x = 0$ and, as (4.12) shows, $\mathrm{d}^2h/\mathrm{d}x^2 = R_s^{-1}$ so that κ_1 becomes

$$\kappa_1 = 1 + \tfrac{2}{3}\mathscr{F}^2\frac{h_1}{R_s}. \tag{4.18}$$

It is emphasized that this result assumes that (4.12) applies, which we see from figure 4 is not the case in the central part of the jump. This will be discussed in further detail later in connection with the analysis of the momentum variation between sections 1 and 2.

In the calculation of κ we have used $\mathscr{F}$ from the measurements using (3.7). The values of κ_1 calculated from (4.18) are also shown in table 2.

For the section at $h_2(x/h_1 = 8)$, we have no information from which κ_2 can be determined. However, since this is far downstream of the jump where $\mathrm{d}h/\mathrm{d}x$ is close to zero, we assume $\kappa_2 \sim 1.0$.

The values of the correction factors along with the measured values of ξ (also listed in table 1) are then used to determine $\mathscr{F}^2$ from (4.8) and these values are also given in table 2. We see that these results for $\mathscr{F}$ are in much closer agreement with $\mathscr{F}$ values determined directly from the measurements using (3.7). The results for jumps 1 and 2 are, in fact, remarkably similar. The agreement between $\mathscr{F}$ (4.8) and $\mathscr{F}$ (3.7) gives basis for expecting that (4.8) includes the major mechanisms active in the jump. On the other hand, the significant difference between these values and $\mathscr{F}'$ determined from the classical expression (4.1) indicates that effects of non-uniform velocities and non-hydrostatic pressure are important.

In all, these results underline the importance of the seemingly small deviations in the experiments from the ideal conditions usually assumed in classical hydraulics.

4.2. *Momentum variation inside the jump*

In general, we should expect the momentum flux M to be constant through all vertical sections of the jump.

As an introductory consideration, it is noted that, when integrating over depth to determine the momentum flux, the turbulent fluctuations of the free surface are included so that the instantaneous depth is $h(x,t) = \widetilde{h(x)} + h'(x,t)$. A related problem has been discussed recently by Brocchini & Peregrine (1996) for the problem of defining mean shorelines on beaches with wave action. Hence, the velocity part of the momentum flux becomes

$$\int_0^{\tilde{h}+h'}\widetilde{(\tilde{u}+u')^2}\,\mathrm{d}z = \int_0^{\tilde{h}}(\tilde{u}^2 + \widetilde{u'^2})\,\mathrm{d}z + \int_{\tilde{h}}^{\tilde{h}+h'}\widetilde{(\tilde{u}+u')^2}\,\mathrm{d}z. \tag{4.19}$$

Here, the last term can be approximated by $2\tilde{u}\widetilde{u'h'} + \widetilde{h'u'^2}$ where the value of the variables are to be taken near the surface. Not enough information is available to assess precisely the value of these terms. However, we know that $h'_{rms} \ll \tilde{h}$ even near the toe of the roller. Furthermore, u'_{rms} at the surface is smaller than u'_{rms} near the lower

edge of the roller which gives the main contribution to the turbulent part of the first integral in (4.19). Hence, it is expected that these terms will be smaller than $\int_0^{\tilde{h}} \widetilde{u'^2}\, dz$, which we will see shortly give negligible contributions to the overall momentum flux. Hence, in the following, we omit the terms due to the turbulent fluctuations of the free surface.

Omitting again the $\widetilde{()}$ over the turbulent averaged quantities, except when ambiguous, we can write the total momentum flux as

$$M(x) = \int_0^{h(x)} \rho(u^2 + \widetilde{u'^2})\, dz + \int_0^{h(x)} p\, dz \tag{4.20}$$

where $\rho\widetilde{u'^2}$ is the turbulent normal stress. We use the term M_1 for the momentum flux through the section at h_1 and $M(x)$ should then satisfy

$$M(x) = M_1 - \int_{x_1}^{x} \left(1 + \frac{2h}{B}\right) \tau_w\, dx. \tag{4.21}$$

Here, the wall friction τ_w has been determined by a simple friction factor formula

$$\tau_w = \tfrac{1}{8}\rho f U^2, \tag{4.22}$$

where f is the friction coefficient. Since the roughness of both bottom and sides of the flume is very small, f is set to 0.01 (see e.g. Henderson 1966).

Estimates of the contribution from the wall shear stresses show that the τ_w-term in (4.21) is $O(10^{-4}\rho U^2 h_1)$ for all three Froude numbers. Hence, the wall friction is negligible in comparison to the other contributions to M.

For the calculation of M, the pressure $p(z)$ is determined from (4.11). In that expression, both w and w' were measured directly and so was uw and $\widetilde{u'w'}$. The contribution to p from $\widetilde{u'w'}$ is small but that is not the case for uw near the front of the jump. The total contribution from p can be written

$$\int_0^{h(x)} p\, dz = \tfrac{1}{2}\rho g h(x)^2 - \int_0^{h} \rho(w^2 + \widetilde{w'^2})\, dz + \int_0^{h} \frac{d}{dx}\left(\int_z^{h} (\rho uw + \widetilde{u'w'})\, dz\right) dz. \tag{4.23}$$

Here, the inner integral in the last term can be evaluated directly from measured quantities, but only along the verticals where measurements were taken. In order to obtain the x-derivatives in that term, spline approximations were developed for the values of the integral of $uw + \widetilde{u'w'}$ in (4.11).

In figure 5, the contribution from the main terms in (4.20) with (4.11) substituted, are plotted for the x positions where measurements were taken. We see that by far the most important terms are the u^2 and the p contributions, whereas the effect of the turbulent normal stresses is only about 1%. The $\widetilde{u'w'}$ contributions to the pressure variation turn out to be small. On the other hand, the w^2 and the uw contributions to $p(z)$ are of some importance, in particular in the roller region. All those terms are included in the p contribution in the figure.

The values of $M(x)$ itself are also shown and we see that M is constant to within about 5%, the largest errors occurring in the roller region.

A possible reason for the inaccuracies in M is associated with the fact that the measurements of $h(x)$ play an important role in the results for M, and there is no information as to how the capacitance wave gauges function for a surface with large turbulent fluctuations, as in the front of the jump.
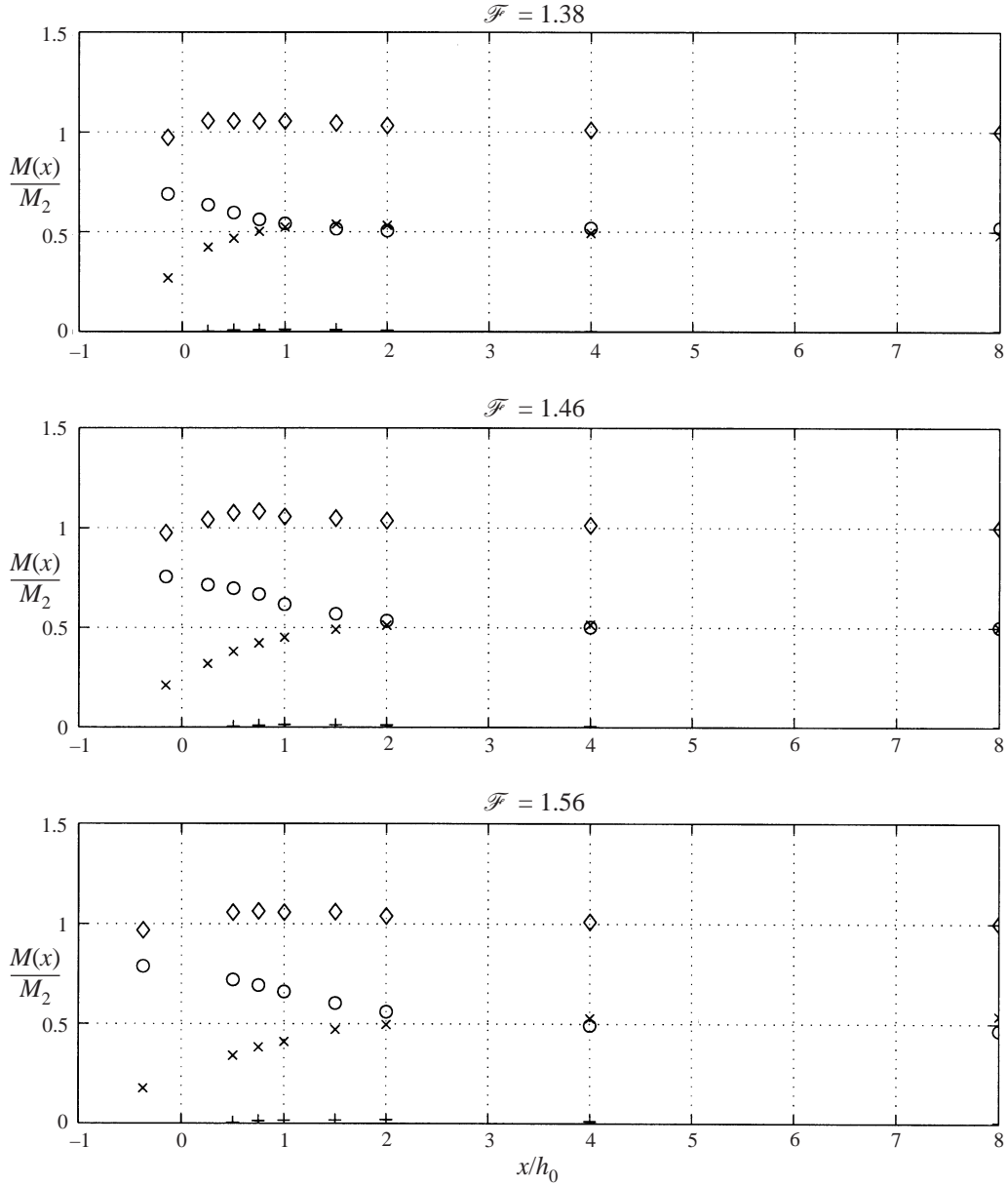
FIGURE 5. Calculated momentum flux $M(x)/M_2$ for the values of x/h_0 along the jump where measurements were taken. $\diamond$, Total momentum; $\times$, pressure contribution; $\circ$, velocity contribution; $+$, turbulent normal stresses.

Hence, for all practical purposes, the momentum flux M may be approximated by

$$M = \rho\alpha(x)\frac{Q^2}{h(x)} + \tfrac{1}{2}\rho g\kappa(x)h(x)^2, \qquad (4.24)$$

where $\alpha(x)$ and $\kappa(x)$ represent the local values of the momentum and pressure correction factors defined by (4.5) and (4.6), respectively. The values of $\alpha(x)$ and $\kappa(x)$ found by the procedure described above are shown in figure 6. It is emphasized that
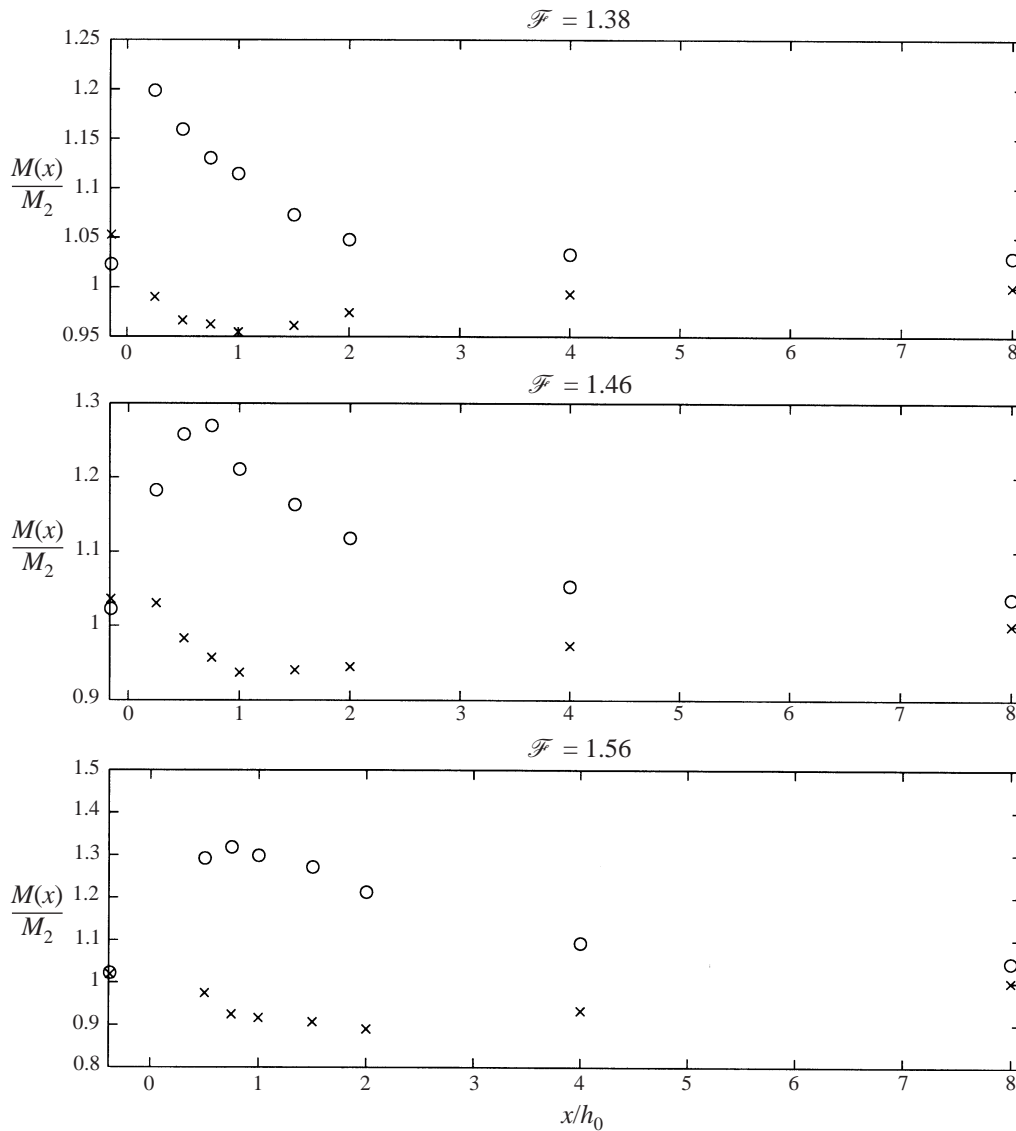
FIGURE 6. $\circ$, α and $\times$, κ values plotted for the values of x/h_0 along the jump where measurements were taken.

whereas the $\alpha(x)$-values in this are fairly accurate, various checks show that the values of $\kappa(x)$ are somewhat less accurate.

It is essential to the connection to breaking waves to realize that $(\alpha - 1)$ and $(\kappa - 1)$ represent the difference between the actual flow and the flow determined from a nonlinear shallow water (NSW) approximation, which would be a model with uniform velocity and hydrostatic pressure distribution everywhere. This difference is obviously generated by the turbulent front with the roller, in addition to the vertical accelerations represented by the curvature of the streamlines. The NSW equations conserve mass, momentum and energy, but the momentum flux anywhere between sections 1 and 2 is smaller than the momentum flux at 1 or 2. The momentum deficit

ΔM defined by

$$\Delta M = M - M_{NSW}, \tag{4.25}$$

is therefore determined as

$$\Delta M = \rho \left((\alpha - 1)\frac{Q^2}{h(x)} + \tfrac{1}{2}g(\kappa - 1)h(x)^2 \right). \tag{4.26}$$

The ΔM is generated by the breaking front and is just large enough to make M constant through the jump and hence prevent the front from steepening further. Conversely, the momentum deficit means that fronts in the NSW models steepen until they become vertical ('breaking' occurs, but at that point the underlying assumptions for the equations are of course no longer valid). It was shown by Svendsen & Madsen, (1984) that adding a ΔM to the NSW equations stabilizes the fronts and extracts energy from the motion. The principle of artificially adding ΔM has been used by Basco & Svendsen (1984) who specified an $\alpha(x)$ distribution to the NSW equations and by Schäffer *et al.* (1993) to establish a Boussinesq model for breaking waves.

The variation of ΔM determined from the measurements is shown in figure 7 along with the surface elevation ζ. The horizontal coordinate is x/h_0 and we see that although ΔM has its maximum close to the toe and inside the roller region, it remains large much further downstream of the end of the actual roller.

It is also useful to discuss how the approximations introduced by Hornung *et al.* (1995, hereinafter referred to as H95) differ from the results found above. H95 uses the assumption that w/U varies linearly from the bottom to the surface for all vertical sections throughout the jump. As the measurements show, these assumptions do not hold in general. The major deviation comes from the fact that, in the roller region, the surface value of u differs substantially from the depth averaged velocity U (see figure 4). The consequence is that the pressure correction factor, implied by Hornung's assumptions, which is given by (4.17), deviates from the value of κ determined from the pressure contributions that we calculate directly from (4.11).

5. Analysis of the flow in the roller

The accurate curve-fits for the horizontal velocity profiles combined with the information about the volume flux in the jump make it possible to determine the lower limit of the roller, because over the roller the net volume flux is zero. Hence, the height h_r of the roller above the bottom satisfies the equation

$$\overline{Q} = \int_0^{h_r} u\, \mathrm{d}z. \tag{5.1}$$

The thickness of the roller is accordingly given by

$$e = h - h_r. \tag{5.2}$$

The values of $e(x)$ found this way have been used to indicate the lower boundary of the roller ($\circ$ in figure 2).

An approximate value for the length ℓ_r of the roller can be obtained by interpolation between the verticals. Figure 8 shows that if we, based on trial and error, consider the variation of $e(x)/h_2\sqrt{\xi}$ versus x/ℓ_r there is a reasonable similarity for all three jumps. It is interesting to note that the roller ends well before the depth reaches its maximum downstream value (see §7).

Another important aspect of the flow is the turbulent stresses generated. The measured data provide information for $\widetilde{u_i'u_j'}$ for all the same points for which mean
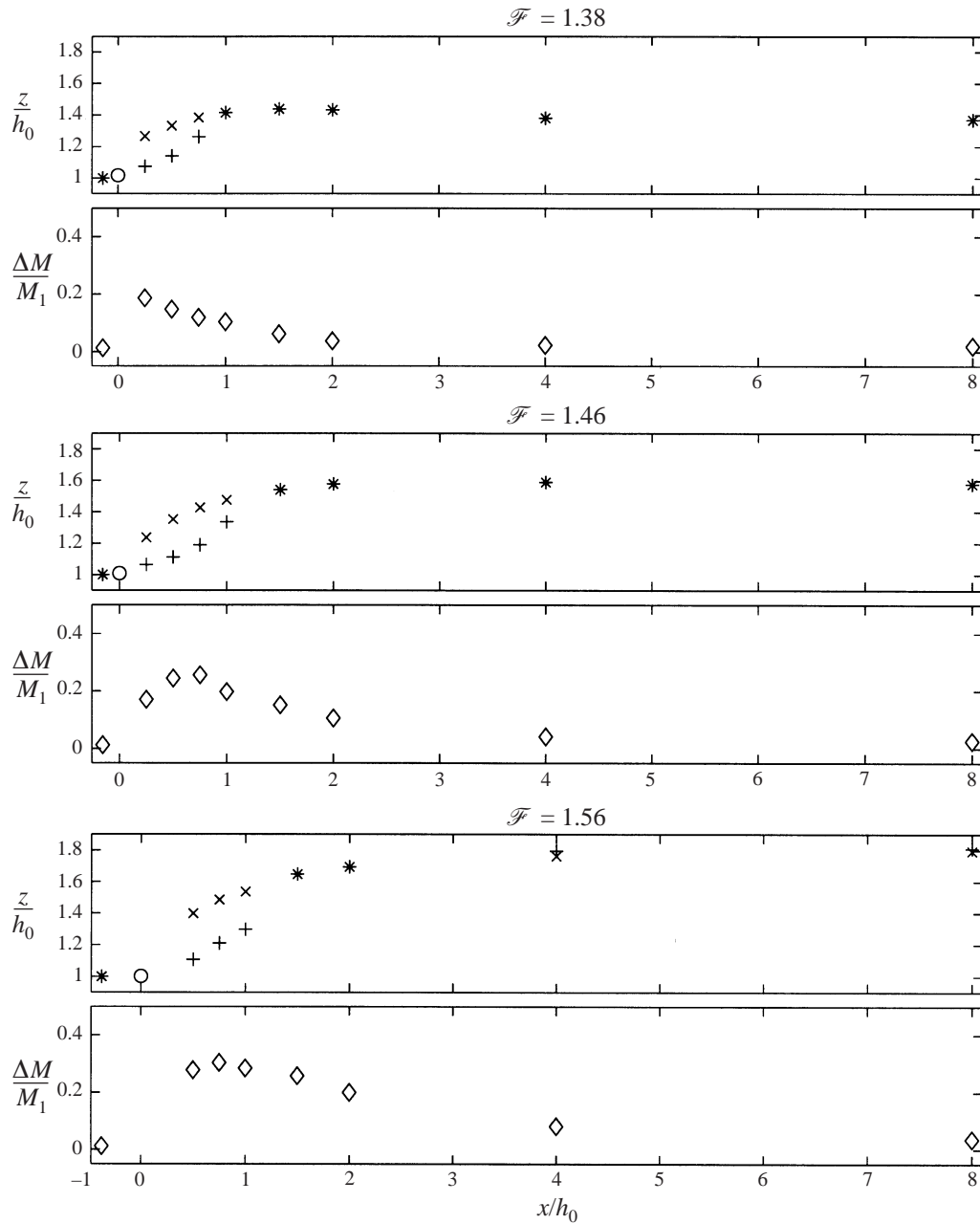
FIGURE 7. The variation of the ×, surface elevation ζ, and $\diamond$, ΔM plotted for the values of x/h_0 along the jump where measurements were taken. +, The location of the dividing streamline (lower limit of roller); $\circ$, the water depth at the toe of the jump.

velocities were obtained. Figure 9 shows the measured values of $\widetilde{u'w'}$ and figure 10 show the values of $(\widetilde{u'^2})^{1/2}$ and $(\widetilde{w'^2})^{1/2}$. As could be expected, the stresses are particularly large in the region underneath and inside the roller. Although measurements were not obtained from the uppermost part of the roller itself, we can get a fair estimate of the τ_{yx}-variation by assuming that the shear stresses along the mean water
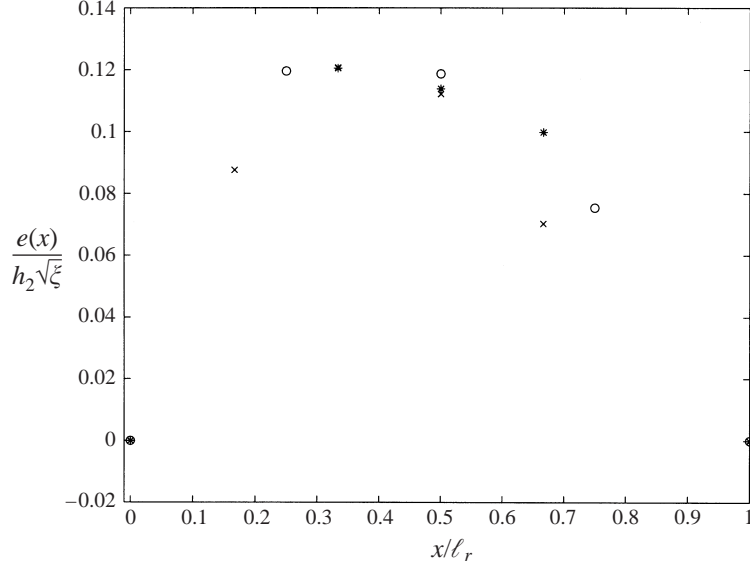
FIGURE 8. Non-dimensional roller thickness $e(x)/h_2\sqrt{\xi}$ versus x/ℓ_r where ℓ_r is the roller length: for $\circ$, $\mathcal{F} = 1.38$; $\times$, $\mathcal{F} = 1.46$; $*$, $\mathcal{F} = 1.56$.

surface are close to zero. An analysis of the momentum balance inside the roller can further illustrate the details of that part of the flow.

For this purpose, we consider the section of the roller shown in figure 11. The upper boundary is the mean water surface, the lower is assumed to be a mean streamline inside the roller. n, s are local coordinates, s being along the dividing streamline that forms the lower boundary at the roller. η is the thickness of the roller in the n-direction. It is assumed that η is much smaller than the length of the roller. This is reasonably supported by figures 7 and 8 from which we can estimate that the ratio e_{max}/l_r is approximately 0.15–0.22. It is also assumed that either the curvature of the dividing streamline is small (as at the centre of the roller) or the momentum flux is small (as at the ends of the roller) to the extent that we can disregard the gradients of the mean momentum fluxes in the mean streamline direction in comparison to other contributions to the momentum balance. The same applies to the gradients of the turbulent momentum fluxes. Analysis of the measurements, where they are available inside the roller, indicated that this is indeed a valid assumption. It is noted from comparison of the figures for the mean velocities and the turbulent fluctuations that, in the roller region, the velocity fluctuations are at least of the same magnitude as the mean velocities, which implies that the instantaneous flow can change direction as in oscillatory flow. Yeh & Mok (1990) discussed the flow in the roller in more detail.

The total velocities in the n, s directions are (v_n, v_s) which we divide into a Reynolds averaged and a fluctuation component by

$$v_\alpha = \widetilde{v_\alpha} + v'_\alpha, \tag{5.3}$$

where α (and β) are used to represent n, s. The total stresses including momentum fluxes are $(\sigma_{nn}, \sigma_{ns}, \sigma_{ss})$, which may be written

$$\sigma_{\alpha\beta} = -p\delta_{\alpha\beta} + \tau_{\alpha\beta} = -p\delta_{\alpha\beta} - \rho\widetilde{v_\alpha v_\beta}. \tag{5.4}$$
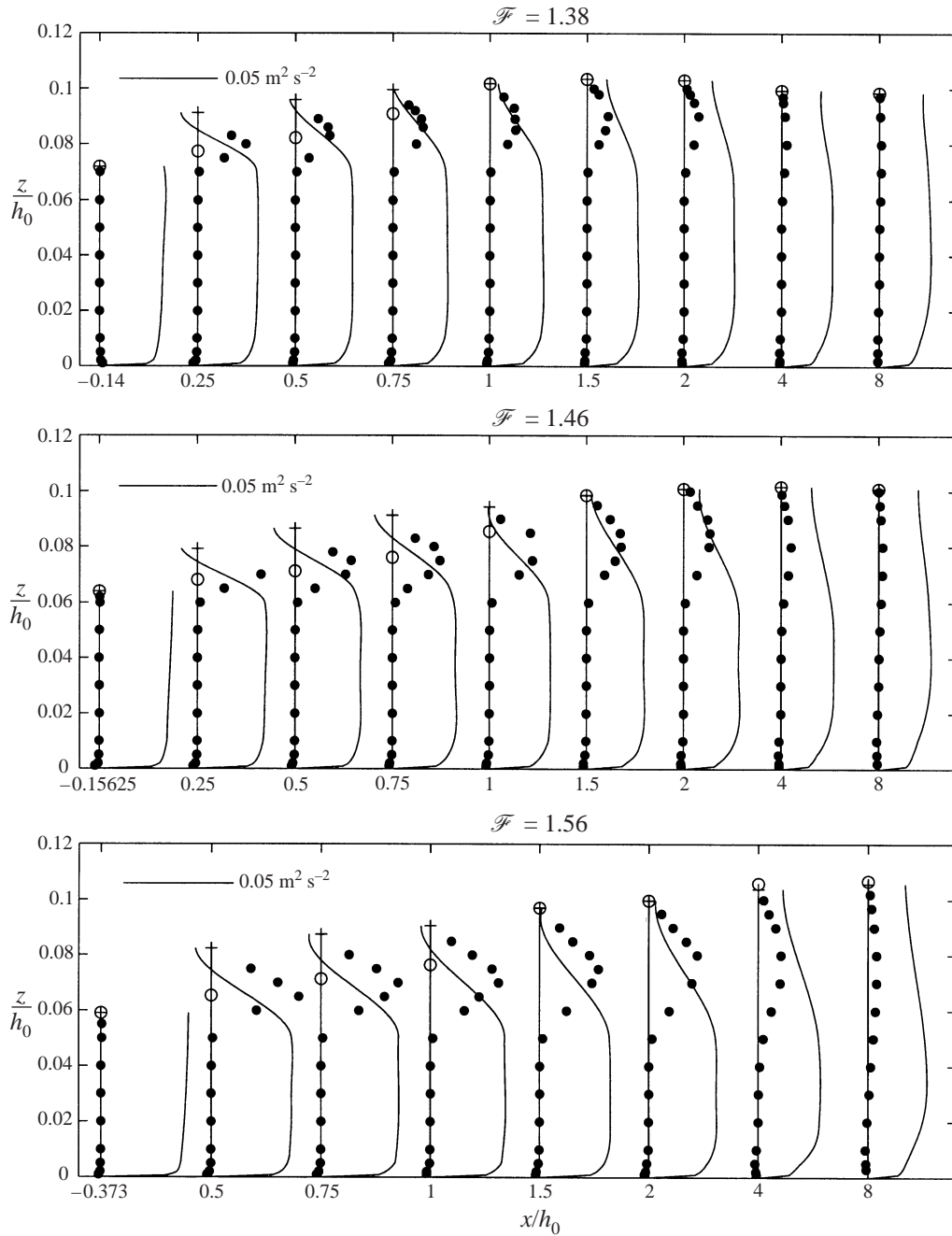
FIGURE 9. •, Measured values of $\widetilde{u'w'}(m^2/s^2)$ plotted for the values of x/h_0 along the jump where measurements were taken; ——, curve-fitted horizontal velocities.

Substituting (5.3) into (5.4), this can also be written

$$\sigma_{\alpha\beta} = -p\delta_{\alpha\beta} - \rho(\tilde{v}_\alpha\tilde{v}_\beta + \widetilde{v'_\alpha v'_\beta}). \tag{5.5}$$

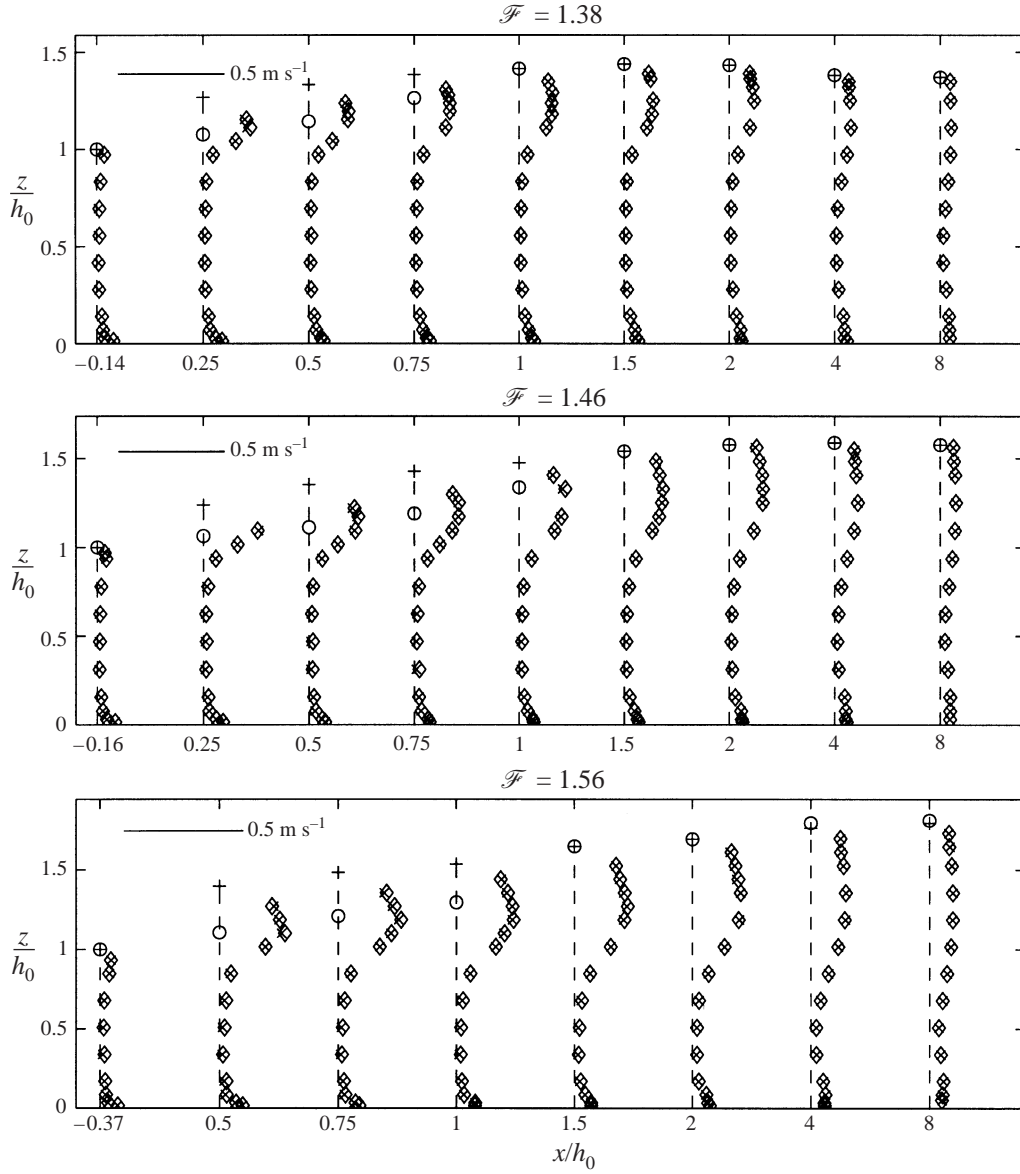The positive directions of the stresses are indicated in figure 11.

FIGURE 10. $\diamond$, Measured values of $\sqrt{\widetilde{u'^2}}$ and $\times$, $\sqrt{\widetilde{w'^2}}$ (m/s) plotted for the values of x/h_0 along the jump where measurements were taken; $\circ$, lower edge of the roller; $+$, water surface elevation.

For steady flow, the conservation of momentum for a control volume between the surface and the variable level n is then

n-direction:

$$-\rho g(\eta - n)\cos\alpha - \sigma_{nn} + \frac{\partial}{\partial s}\int_n^\eta \sigma_{ns}\,\mathrm{d}n = 0, \qquad (5.6)$$

s-direction:

$$-\rho g(\eta - n)\sin\alpha + \frac{\partial}{\partial s}\int_n^\eta \sigma_{ss}\,\mathrm{d}n - \sigma_{ns} = 0. \qquad (5.7)$$
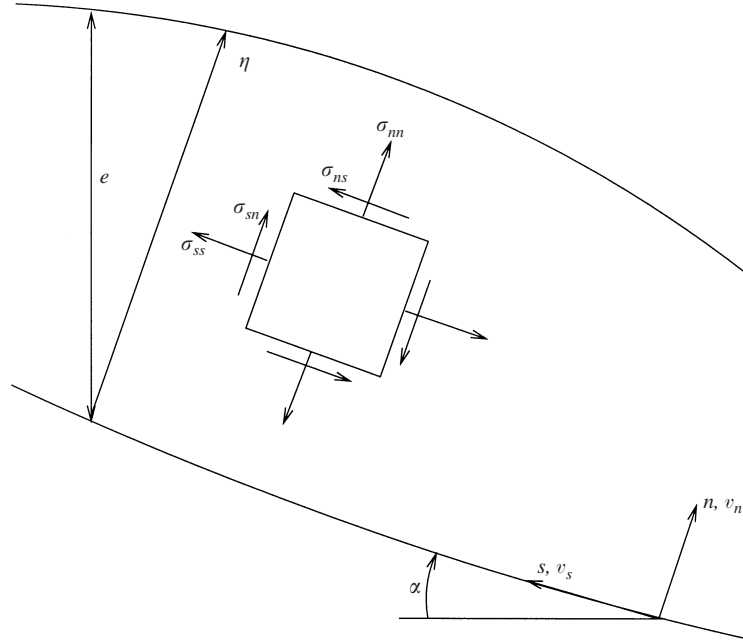
FIGURE 11. Definition sketch for the analysis of the momentum variation
and the stresses in the roller.

It is consistent with the assumption about slow horizontal variation of the flow in
the roller to assume $\widetilde{v_n} = 0$. Using (5.5) we then obtain from 5.6 and (5.7)
n-direction:

$$p(n) = \rho g(\eta - n)\cos\alpha - \rho\widetilde{v_n'^2} + \frac{\partial}{\partial s}\int_n^\eta \rho\widetilde{v_n'v_s'}\,\mathrm{d}n, \tag{5.8}$$

s-direction:

$$\sigma_{ns} = -\rho g\sin\alpha(\eta - n) - \frac{\partial}{\partial s}\int_n^\eta (p - \rho(\tilde{v_s}^2 + \widetilde{v_s'^2}))\,\mathrm{d}n. \tag{5.9}$$

Here, p can be eliminated by integrating (5.8) from n to the surface. As mentioned
above, it turns out from analysis of the measurements that we can disregard the
gradients of the momentum fluxes in the s-direction, which means the last term in
(5.8) is small. We therefore obtain

$$\int_n^\eta p\,\mathrm{d}n \simeq \tfrac{1}{2}\rho g\cos\alpha(\eta - n)^2 - \rho\int_n^\eta \widetilde{v_n'^2}\,\mathrm{d}n, \tag{5.10}$$

which substituted into (5.9) yields

$$\sigma_{ns} \simeq -\rho g\left[\sin\alpha(\eta - n) - \tfrac{1}{2}\frac{\partial}{\partial s}\cos\alpha(\eta - n)^2\right] - \rho\frac{\partial}{\partial s}\int_n^\eta (\tilde{v_s}^2 + (\widetilde{v_s'^2} - \widetilde{v_n'^2}))\,\mathrm{d}n. \tag{5.11}$$

The measurements also show, however, that in the roller $\widetilde{u'^2} \sim \widetilde{w'^2}$ (see figure 10) so

that the expression for σ_{ns} simplifies to

$$\sigma_{ns} \simeq -\rho g \left[\sin \alpha (\eta - n) - \tfrac{1}{2} \frac{\partial}{\partial s} \cos \alpha (\eta - n)^2 \right] - \rho \frac{\partial}{\partial s} \int_n^\eta (\tilde{v_s}^2) \, \mathrm{d}n. \tag{5.12}$$

The stresses in the n, s directions can be expressed in terms of the Reynolds stresses τ_{ij} in the x, z directions (which are the measured Reynolds stresses) by the relations

$$\sigma_{nn} = -p + \tau_{xz} \sin 2\alpha - \tfrac{1}{2}(\tau_{xx} - \tau_{zz}) \cos 2\alpha + \tfrac{1}{2}(\tau_{xx} + \tau_{zz}), \tag{5.13}$$

$$\sigma_{ns} = \tfrac{1}{2}(\tau_{xx} - \tau_{zz}) \sin 2\alpha + \tau_{zx} \cos 2\alpha, \tag{5.14}$$

and similarly by replacing α by $\alpha + \tfrac{1}{2}\pi$

$$\sigma_{ss} = -p - \tau_{xz} \sin 2\alpha + \tfrac{1}{2}(\tau_{xx} - \tau_{zz}) \cos 2\alpha + \tfrac{1}{2}(\tau_{xx} + \tau_{zz}). \tag{5.15}$$

The τ_{xx}, τ_{zz} and τ_{xz} are given by $\tau_{ij} = -\rho \widetilde{u_i' u_j'}$. Hence, we can write (5.13)–(5.15) as

$$\sigma_{nn} = -p - \rho \widetilde{u'w'} \sin 2\alpha + \tfrac{1}{2}\rho(\widetilde{u'^2} - \widetilde{w'^2}) \cos 2\alpha - \tfrac{1}{2}\rho(\widetilde{u'^2} + \widetilde{w'^2}), \tag{5.16}$$

$$\sigma_{ns} = -\tfrac{1}{2}\rho(\widetilde{u'^2} - \widetilde{w'^2}) \sin 2\alpha - \rho \widetilde{u'w'} \cos 2\alpha, \tag{5.17}$$

$$\sigma_{ss} = -p + \rho \widetilde{u'w'} \sin 2\alpha - \tfrac{1}{2}\rho(\widetilde{u'^2} - \widetilde{w'^2}) \cos 2\alpha - \tfrac{1}{2}\rho(\widetilde{u'^2} + \widetilde{w'^2}), \tag{5.18}$$

where again $\widetilde{u'^2} \sim \widetilde{w'^2}$ so that

$$\sigma_{nn} = -p - \rho \widetilde{u'w'} \sin 2\alpha - \rho \widetilde{u'^2}, \tag{5.19}$$

$$\sigma_{ns} = -\rho \widetilde{u'w'} \cos 2\alpha, \tag{5.20}$$

$$\sigma_{ss} = -p + \rho \widetilde{u'w'} \sin 2\alpha - \rho \widetilde{u'^2}. \tag{5.21}$$

Combining (5.19) and (5.8) and again neglecting the $\partial/\partial s$-term, we see that p can be written

$$p = \rho g(\eta - n) \cos \alpha - \rho \widetilde{u'w'} \sin 2\alpha - \rho \widetilde{u'^2}, \tag{5.22}$$

which shows that in the roller we do not have simple hydrostatic pressure based on the vertical thickness of the roller as assumed by e.g. Deigaard & Fredsøe (1989).

Though the first term in (5.12) is the largest, it turns out that all three terms contribute to the result, the $\partial/\partial s$ terms in particular in the sections close to the ends of the roller where the thickness varies more rapidly.

Results from calculations with (5.12) for the variation in the n-direction of $\sigma_{ns}/\rho U_1^2$ (where U_1 is the mean velocity at h_1) are shown in figure 12. The ordinate is n/η and we see that the predicted values are close to the measured, which are marked by $\circ$.

It is interesting to compare the shear stresses at the lower edge of the roller ($n = 0$) with the simplified expression which is obtained if we assume hydrostatic pressure in the roller

$$\tau_r = \rho g \eta \tan \alpha_s / \cos \alpha_s, \tag{5.23}$$

where α_s is the surface slope. This expression has been suggested as an estimate for σ_{ns} (Deigaard & Fredsøe 1989), and is frequently used in the literature. The comparison with (5.12) for $n = 0$ and with the measurements along the dividing streamline are shown in figure 13.

We see that over most of the roller, (5.12) gives a good prediction of the shear stress σ_{ns} along the dividing streamline. The only point where there is a significant
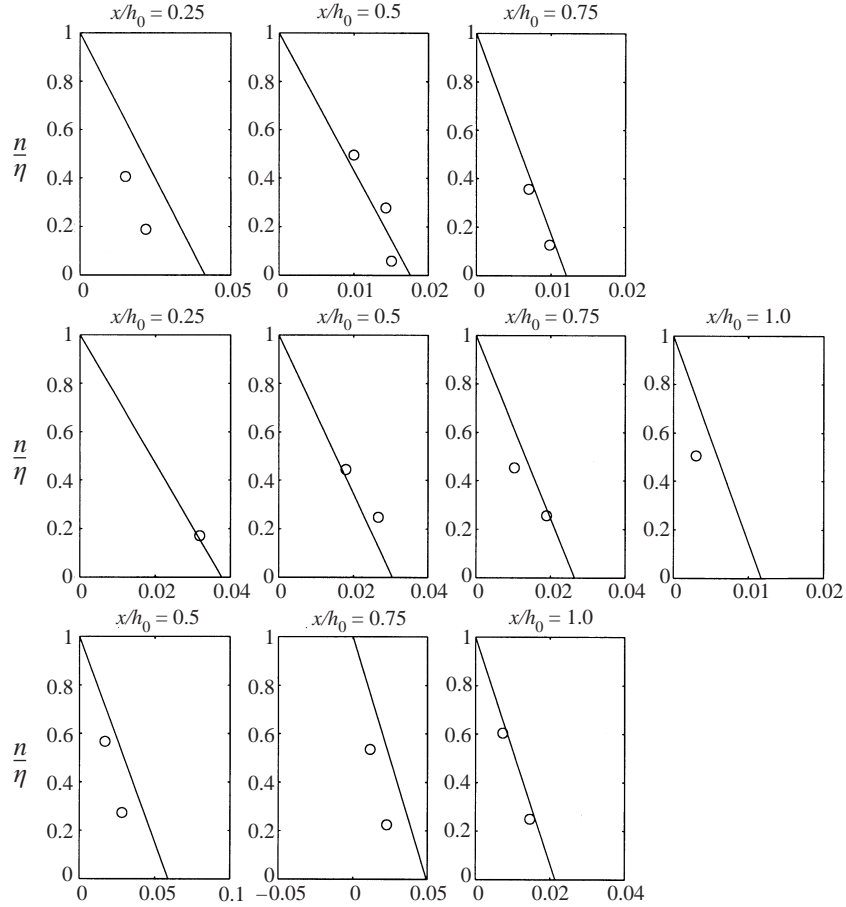
FIGURE 12. Variation of the shear stresses $\sigma_{ns}/\rho U_1^2$ (horizontal axis) in the n-direction across the roller for the values of x/h_0 in the roller region where measurements were taken. The top row is for $\mathscr{F} = 1.38$, the middle row is for $\mathscr{F} = 1.46$ and the bottom row is for $\mathscr{F} = 1.56$.

deviation is the first measuring point in each jump where (5.12) tends to overpredict the magnitude of σ_{ns}.

On the other hand, we also see that (5.23) overpredicts σ_{ns} by as much as a factor of 2 in particular in the second half of the roller.

Finally, figure 14 shows that, measured in terms of ρU_1^2 versus x/ℓ_r, the shear stresses along the dividing streamline in the three hydraulic jumps considered, largely exhibit the same variation over the length of the roller. This similarity is equivalent to the similarity found for the variation of the vertical roller thickness e (see figure 7) and may of course not apply for jumps with significantly larger $\mathscr{F}$ values.

6. Vorticity, stresses, and eddy viscosity

It is also of significant interest to analyse the development of the vorticity of the flow. The vorticity

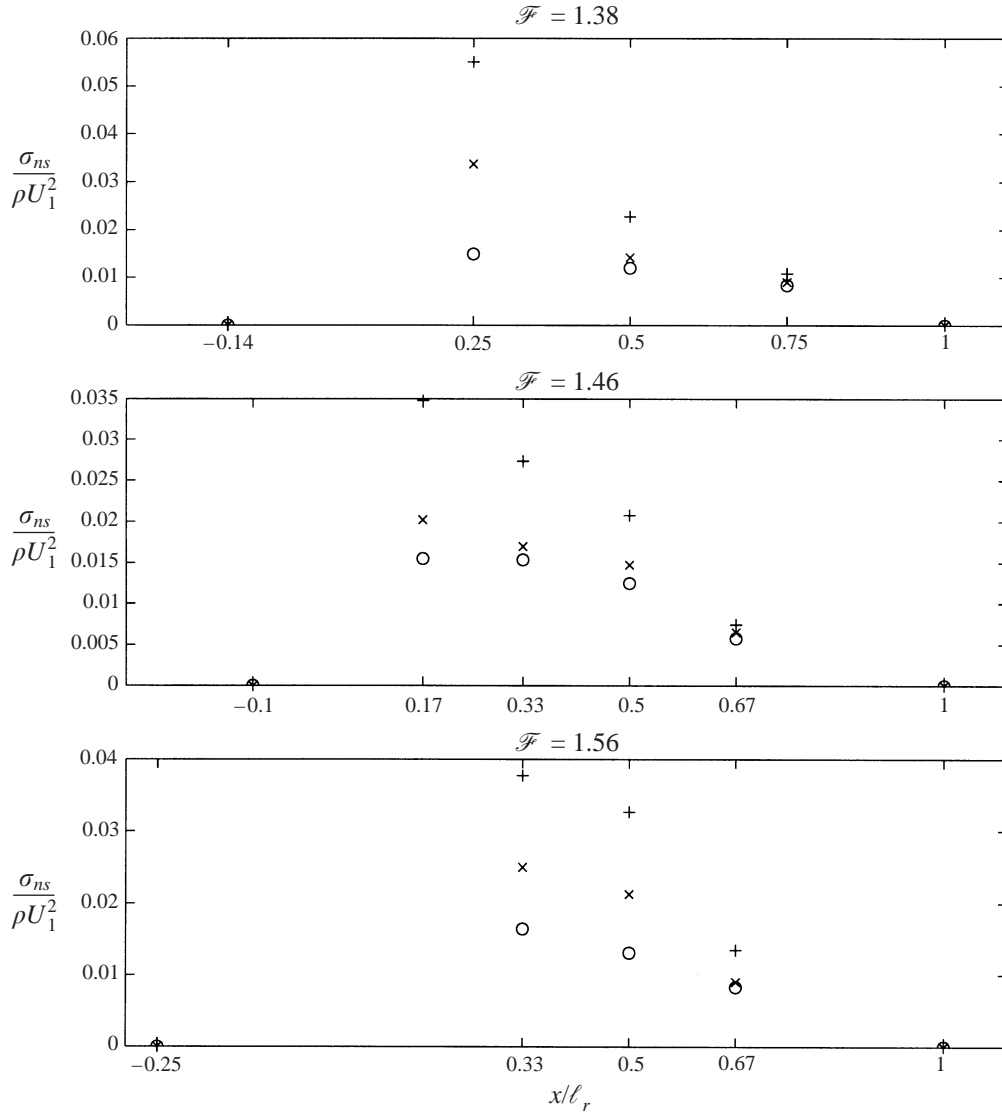$$w = \frac{\partial u}{\partial z} - \frac{\partial w}{\partial x}, \tag{6.1}$$

FIGURE 13. Variation of $\sigma_{ns}/\rho U_1^2$ (vertical) versus x/ℓ_r along the lower limit of the roller (at $n = 0$): $\circ$, measurements (interpolated values); $\times$, obtained from (5.12); $+$, from (5.23).

is obtained from the curve-fitted measured velocities. Since measurements were obtained along only a few verticals, it requires some care to determine $\partial w/\partial x$. However, as figure 4 shows, the vertical velocities are small and vary relatively slowly in the x direction which is also qualitatively confirmed by a comparison of figures 3 and 4. It was found that the values of $\partial w/\partial x$ were negligible in comparison to $\partial u/\partial z$. Figure 15 shows the vorticity along the verticals where measurements were taken.

Qualitatively, the results confirm the patterns for the breaking waves behind a hydrofoil found by Lin & Rockwell (1995) in those of their cases where the breakers were strong enough that capillary effects were negligible. A quantitative comparison is difficult, however, because generating conditions for the two flows are so different.
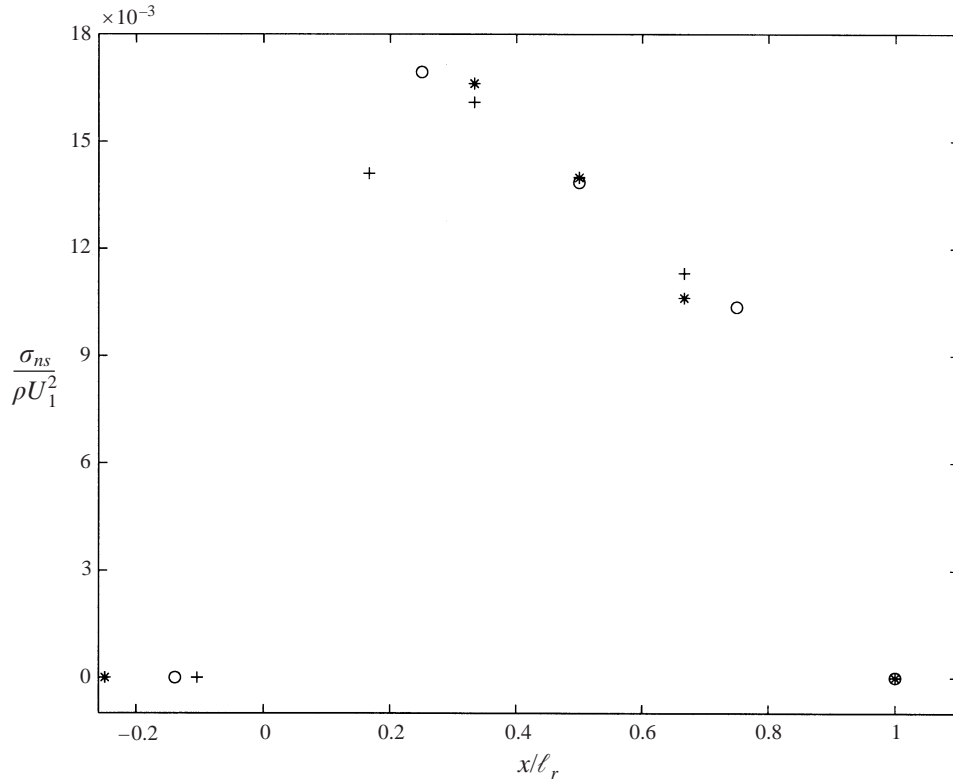
FIGURE 14. Non-dimensional shear stresses $\sigma_{ns}/\rho U_1^2$ (vertical) versus x/ℓ_r along the lower limit of the roller for $\circ$, $\mathscr{F} = 1.38$; $\times$, $\mathscr{F} = 1.46$; $*$, $\mathscr{F} = 1.56$.

It is clear that vorticity generation is initiated at the toe of the turbulent front where the high-speed flow along the incoming free-surface streamline meets the fluid which is slowly moving down along the surface of the roller. Because of the high speed, the incoming flow seems to continue undisturbed over a short distance underneath the roller. By careful observation, it can be seen that the first very short part of the roller essentially floats on the incoming high-speed fluid over what seems to be a very thin highly aerated layer where all the shear is located.

The momentum balance for the flow around the toe was discussed by Svendsen & Madsen (1984) who pointed out that, in spite of the fact that with the described picture of the flow the shear at the toe becomes theoretically infinitely large, the shear stress must for dynamical reasons remain bounded at the toe (and in fact must go to zero as $e \to 0$). This can be accomplished by assuming that the effective (turbulent) viscosity v_t goes to zero faster than the shear. If we think of v_t as being $\ell\sqrt{k}$, this is in accordance with the fact that both the length scale and the kinetic energy must start at zero values at the toe.

A short distance into the roller, the incoming flow becomes unstable and the mean incoming streamline becomes the centre in a flow pattern that has resemblances of a mixing layer (Peregrine & Svendsen 1978). As the mixing develops, the magnitude of the fluctuations develop to a size that is comparable to the thickness of the roller and start interacting with the free surface. This occurs in the central part of the roller and that is undoubtedly the area where the strongest production of turbulence takes place.
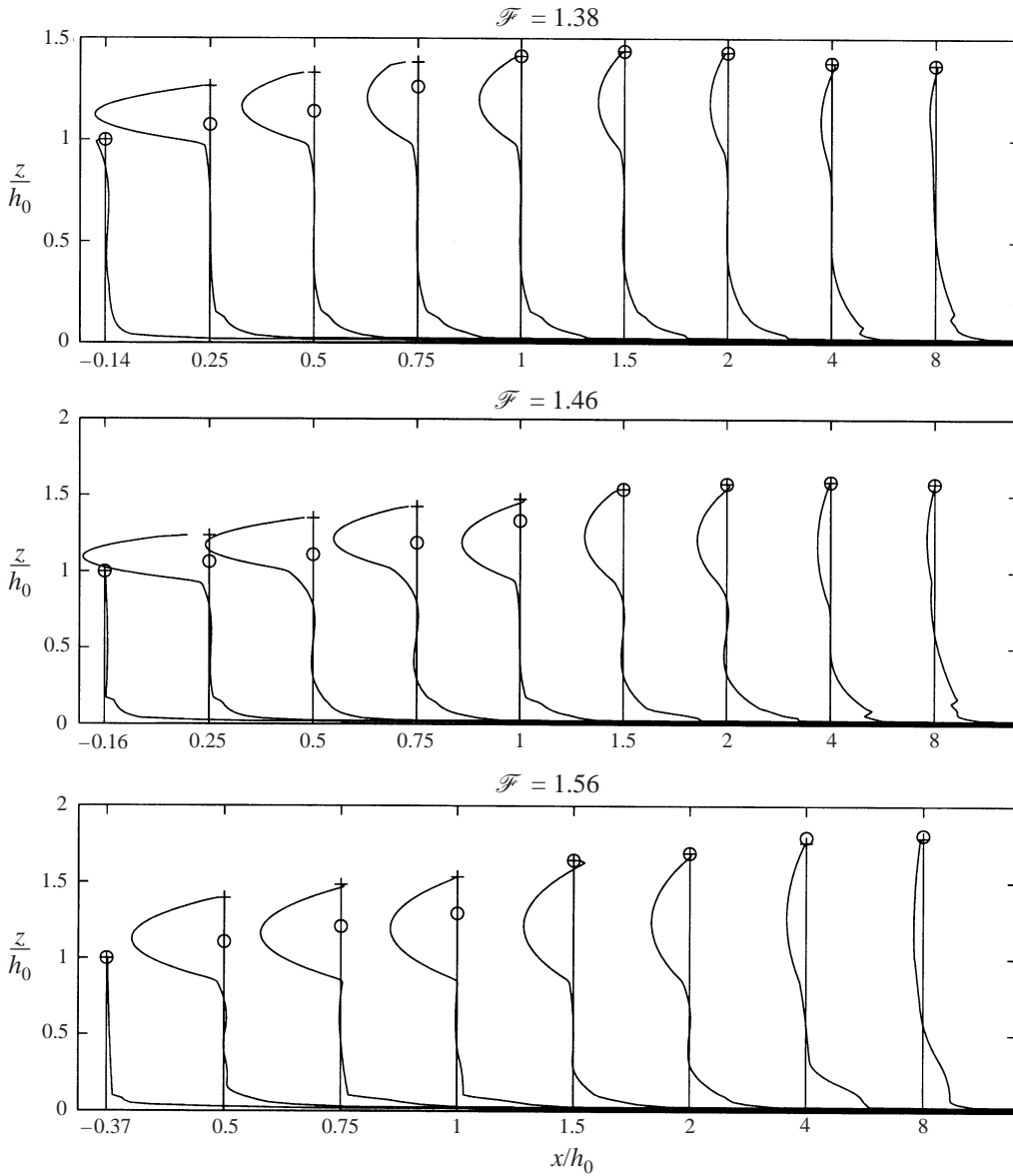
FIGURE 15. The vorticity distributions determined from the measurements plotted for the values of x/h_0 along the jump where measurements were taken.

It is interesting that along the streamline that divides the roller with recirculating flow from the rest of the flow which essentially is unidirectional, the vorticity in all three jumps seems to follow the same dimensionless variation. This is illustrated in figure 16 which shows values of $\omega' = \omega h_2 \xi / U_1$ versus x/ℓ_r where ℓ_r is the roller length. ω' increases rapidly from the toe to a maximum which is reached about 10% of ℓ_r into the roller. From there, the vorticity decreases almost linearly to the zero value at the end of the roller where the dividing streamline meets the free surface.

To some extent, it is confirmed that the flow has many resemblances with a shear layer positioned along the streamline. We see from figures 9 and 15 that immediately
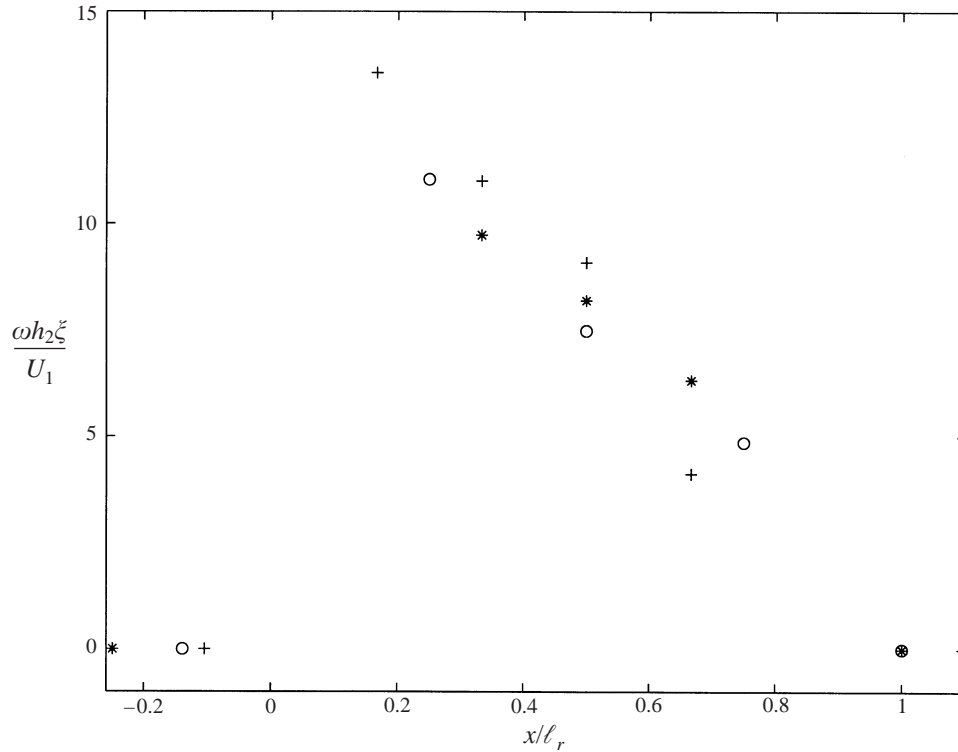
FIGURE 16. Dimensionless vorticity $\omega' = \omega h_2 \xi / U_1$ (vertical) versus x/ℓ_r along the lower limit of the roller for $\circ$, $\mathscr{F} = 1.38$; $\times$, $\mathscr{F} = 1.46$; $*$, $\mathscr{F} = 1.56$.

downstream from the toe of the roller, both the shear stresses and the vorticity are maximum along the dividing streamline. Figure 16 also indicates that the strength of the vorticity decreases over the roller length. Those features have similarities with the characteristics of a shear layer with symmetry axis near the lower limit of the roller. In a shear layer, the vorticity would spread symmetrically downward and upward by diffusive mechanisms (mainly turbulent mixing). Spreading is also found to happen, but not symmetrically. The turbulence above the dividing streamline is so strong that the vorticity is spread over the entire roller region from the very beginning at the toe. Furthermore, the fluid domain above is limited by the presence of the free surface (see figure 15). The difference in diffusivity between the roller and the region below the dividing streamline is probably why, towards the downstream end of the roller where the lower limit of the roller bends upward toward the free surface, the maximum values of both ω (figure 16) and $\widetilde{u'w'}$ (figure 9) occur below the lower limit of the roller and further downstream well below the surface (i.e. 'inside' the flow).

Eventually, sufficiently far downstream, the flow will attain the characteristics of a (nearly) uniform open channel flow dominated by the bottom-generated turbulence and friction. Note, however, from figure 15, that even at $x/h_0 = 8$ this point of equilibrium is not quite reached yet. There is still residual vorticity from the roller and the bottom boundary layer has only spread over 40–50% of the full depth.

We also see that, although the results for the vorticity for the upper part of the roller are based on the extrapolations of the curve-fitted velocity profiles, the variations of ω over the roller are reasonable. In the interpretation, we have made
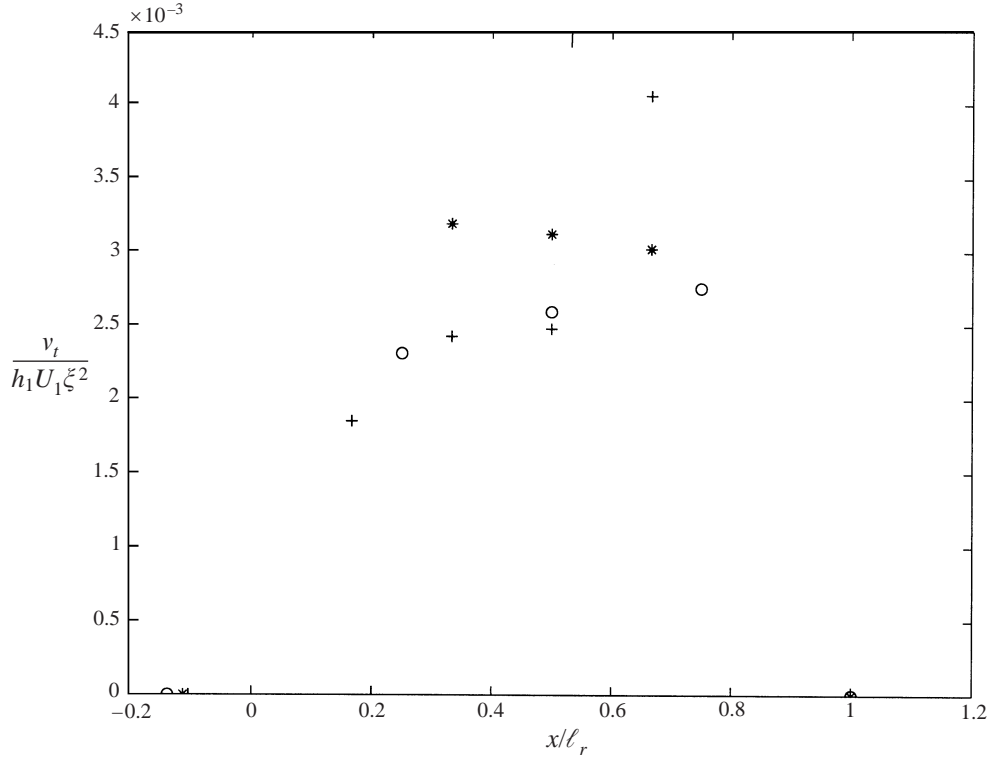
FIGURE 17. The dimensionless eddy viscosity $v_t/(h_1 U_1 \xi^2)$ versus x/ℓ_r along the lower limit of the roller for $\circ$, $\mathscr{F} = 1.38$; $\times$, $\mathscr{F} = 1.46$; $*$, $\mathscr{F} = 1.56$.

the assumption that the gradient of the velocity and the value of the vorticity are zero at the mean water surface. In reality, neither the velocity gradients nor the shear stresses or the vorticities will be exactly zero at the mean water surface. A small part of the deviation from this assumption would be due to the surface boundary layer induced by the zero stresses at the instantaneous free surface. More importantly, however, using the turbulent averaged mean water surface as surface boundary will generate non-zero Reynolds contributions to the averages at the mean surface. The problem was probably first discussed by Hasselmann (1971) and lately by Brocchini & Peregrine (1996). Unfortunately, the available measurements do not provide sufficient information to analyse the details. It is expected that the contributions are relatively insignificant in comparison to the stresses and vorticity in the lower part of the roller.

It is also seen that, in spite of the smooth bottom, the bottom boundary layer produces a fair amount of vorticity, and in fact also a fair amount of turbulent kinetic energy.

Finally, if the shear stress at the bottom of the roller scale as $\tau/\rho U_1^2$, and the vorticity is close to $\partial u/\partial z$ and scales as $\omega h_2 \xi/U_1$, it would be expected that the eddy viscosity along the roller bottom would scale as $v_t/(h_1 U_1 \xi^2)$. Figure 17 shows a plot of $v_t/(h_1 U_1 \xi^2)$ versus x/ℓ_r along the lower edge of the roller. It is clear that there is considerably more scatter than in the two previous plots and more data would be useful.

It is also possible from the measurements of velocities and shear stresses to obtain an estimate for a value of the eddy viscosity v_t over the entire vertical at each x where
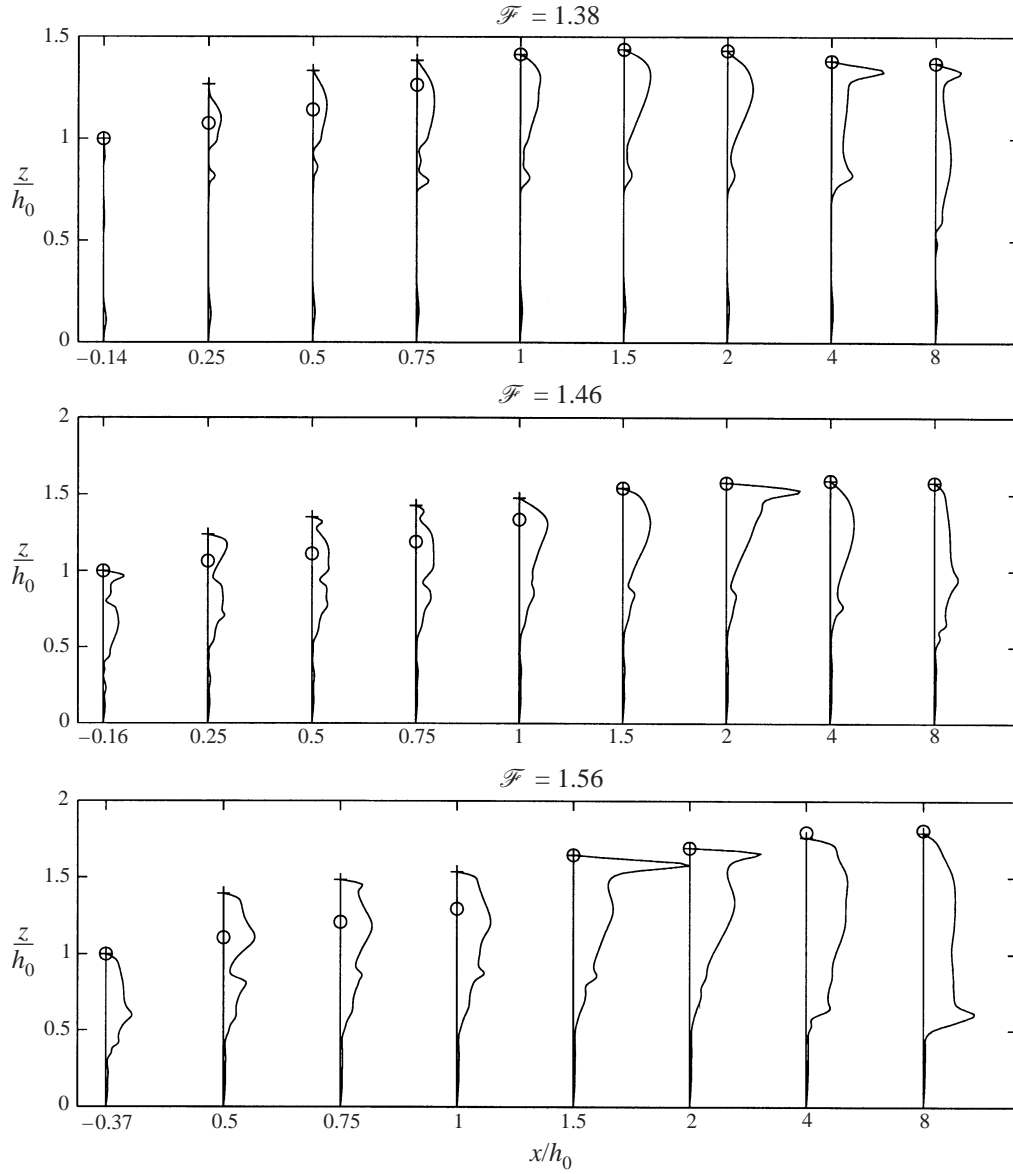
FIGURE 18. The eddy viscosity variations determined from the measured shear stresses and the calculated vertical velocity gradients.

measurements were taken. Assuming v_t is defined by the equation $\tau_{zx} = \rho v_t \partial u / \partial z$, we obtain the values shown in figure 18 for v_t. To avoid the singularities for $\tau = 0$ in the computation for this figure, we set $v_t = 0$ when τ becomes sufficiently small.

7. The angular momentum balance

Recently, the angular momentum balance for hydraulic jumps was discussed in H95. It is obvious from the outset that just as linear momentum is conserved, so is angular momentum. The question is what are the major contributions to the angular momen-

tum balance. It turns out that, in particular, the contribution from non-hydrostatic pressures is an important element of uncertainty in that balance. As mentioned in §4, H95 calculated that contribution by assuming that the vertical velocity everywhere varied linearly from bottom to surface (see (4.12)). This assumption is not satisfied inside the jump, and particularly not in the region where the effect of the vertical velocities on the pressure distribution is most significant. In calculating the vertical velocity they used the depth-averaged horizontal velocity.

These assumptions, however, made it possible to give a simple analytical expression for the non-hydrostatic pressure which is given by (4.15) and through that for the contribution of the vertical accelerations to the angular momentum balance. This contribution comes from the pressure variation on the bottom. In order to balance the angular momentum, however, H95 also assumed that the downstream horizontal velocity in the jump varied linearly over depth with a constant negative vorticity, Ω. They then determined the value of Ω required to satisfy the angular momentum balance.

Under the normal hydraulics conditions of uniform flow, however, we would expect that the velocity profile sufficiently far downstream of a hydraulic jump will eventually develop to a form that is approximately represented by a logarithmic profile. Such a profile has a distinctive positive vorticity (though not constant over depth). Hence, it is obvious that the analysis of H95 does not apply to such conditions.

The experiments conducted by H95 to verify their analysis were for a bore propagating into quiescent water. However, an assumption of a constant vorticity downstream would not be a reasonable assumption for that flow situation either. With virtually no disturbance from the bottom-generated turbulence, the vorticity generated in a bore would still retain a maximum around the level of the lower edge of the roller. As we move downstream this concentration of vorticity would diffuse upward toward the surface and downward toward the bottom. In fact, figure 15 can give a reasonable estimate of what happens in a bore if we disregard the bottom-generated vorticity in that figure, because (apart from the bottom boundary layer) vorticity is invariant to the coordinate transformation that changes the hydraulic jump to a bore. The following analysis is based on the measurements and analysis that are described in the earlier sections of the paper. For the angular momentum A around a point in the bottom (arbitrary, but for clarity chosen at x_1 at $h = h_1$) we obtain

$$A(x) = \int_0^{h_1} (p + \rho u^2)z \, \mathrm{d}z - \int_0^{h(x)} (p + \rho u^2)z \, \mathrm{d}z - \int_{x_1}^{x} [p - \rho g h(x)]x \, \mathrm{d}x$$
$$+ \int_0^{h(x)} \rho(uw + \widetilde{u'w'})x \, \mathrm{d}z, \quad (7.1)$$

and the expectation would be that $A \equiv 0$ for all x. In the expression (7.1), the pressures along the vertical sections at 1 and 2 are determined from (4.11) and the values of uw and $u'w'$ are also determined directly from the measurements along the verticals. The pressure p along the bottom in the third integral is evaluated by the procedure described in §4 in which spline-fits are used to interpolate between the x-value for which detailed measurements were made.

For illustration, the balance described by (7.1) is evaluated for all the vertical sections out to $x/h_1 = 8$, and the results are shown in figure 19 for all three jumps.

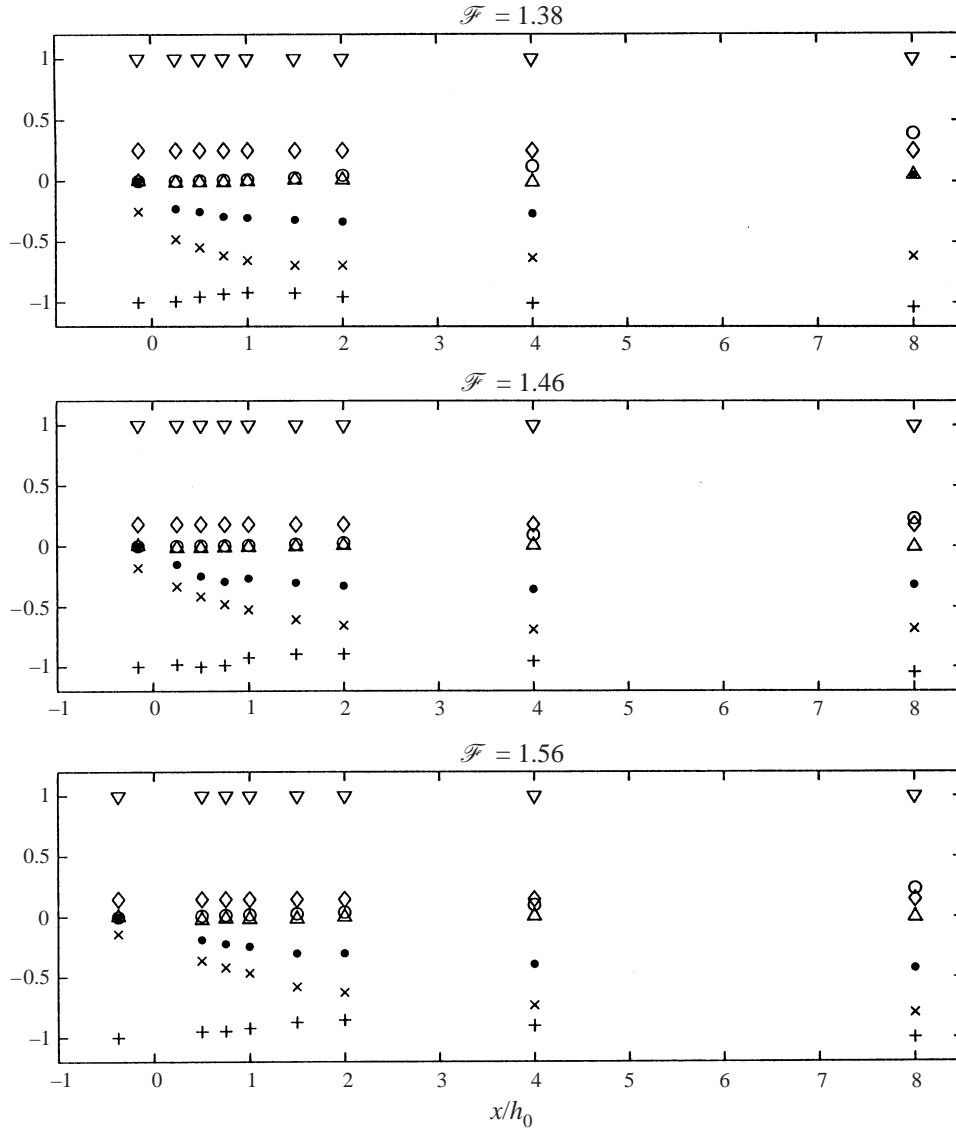We first notice that even at the section at $x/h_1 = 8$ the velocity profile still has

FIGURE 19. Contributions from the terms in (7.1) to the angular momentum balance plotted for the values of x/h_0 along the jump where measurements were taken. The vertical axis has been normalized by $(U_1 h_1)^2/2$. ∇, $\int_{h_1} u^2 z \, dz$; $\diamond$, $\int_{h_1} pz \, dz$; $+$, $\int_{h(x)} u^2 z \, dz$; $\times$, $\int_{h(x)} pz \, dz$; $\triangle$, $\int_{h(x)} uvx \, dz$; $\circ$, $\int_x p_b x \, dx$; $\bullet$, A, the total angular momentum at each section.

not developed to the logarithmic equilibrium profile that is expected 'far downstream' (see figure 2).

Secondly, figure 19 shows that all the terms in (7.1) give significant contributions to the angular momentum balance except the vertical shear stresses at the right-hand section at x. However, those shear stresses are included in the balance since they are also non-zero in the logarithmic profile far downstream. It is therefore evident that for sufficiently large x-values, they will eventually become important, and, as can readily be certified, they are an important component in the angular momentum balance for

steady uniform flow in a rectangular channel. Note also that the contribution from the deviation from hydrostatic pressure on the bottom is non-negligible.

It is obvious that the final result for $A(x)$ is formed as a small (ideally zero) difference between several large numbers. It is therefore not so surprising that, in spite of all efforts, the total angular momentum A is not quite zero. Some of the reasons for that are probably inaccuracies in the measurements, however small, including the measurements of the surface elevation in the roller region. Some are inaccuracies in the spline interpolation procedure we have had to use for the non-hydrostatic contribution to the pressure. As mentioned earlier, we suspect that our estimates of this term are less accurate than the other terms. In all, however, the analysis is expected to show a reasonably accurate picture of the contributions to the angular momentum balance.

8. Conclusions

Detailed LDV-measurements of the flow in three turbulent hydraulic jumps have been analysed. It is found that deviations from uniform velocities and hydrostatic pressure distributions give important contributions to the horizontal momentum balance. At the surface, a model for the flow in the roller gives good agreement with measured stresses and it is shown that results from the simpler model presented by Deigaard & Fredsøe (1989) are misleading. The distribution of vorticity and shear stresses inside the jump give qualitative confirmation of the hypothesis that the breaking resembles a shear-layer but also clearly illustrate the deviations from the flow in ordinary shear layers. Finally, the angular momentum balance has been analysed and it is shown that the assumptions made in H95 do not hold. It is found that dimensionless forms of a number of the variables in the jumps, such as the thickness of the roller, the shear stress, the vorticity, and the eddy viscosity along the lower limit of the roller have shown variations that are independent of the Froude number.

REFERENCES

BAKUNIN, J. 1995 Experimental study of hydraulic jumps in low Froude number range. Center for Applied Coastal Research, University of Delaware, Newark, DE 19711.

BANNER, M. L. & PHILLIPS, O. M. 1974 On the incipient breaking of small scale waves. *J. Fluid Mech.* **65**, 647–656.

BASCO, D. R. & SVENDSEN, I. A. 1984 Modelling turbulent bore propagation in the surf zone. *Proc. 19th Intl Conf. Coastal Engng*, Chap. 7, pp. 99–114.

BATTJES, J. & SAKAI, T. 1981 Velocity field in a steady breaker. *J. Fluid Mech.* **111**, 421–437.

BOWLES, R. I. & SMITH, F. T. 1992 The standing hydraulic jump: Theory, computations and comparisons with experiments. *J. Fluid Mech.* **242**, 145–168.

BROCCHINI, M. & PEREGRINE, D. H. 1996 Integral flow properties of the swash zone and averaging. *J. Fluid Mech.* **317**, 241–273.

BROCCHINI, M. & PEREGRINE, D. H. 1998 The modelling of a spilling breaker: strong turbulence at a free surface. *Proc. 26th Intl Conf. Coastal Engng*, pp. 72–85.

DABIRI, D. & GHARIB, M. 1997 Experimental investigation of the vorticity generation within a spilling water wave. *J. Fluid Mech.* **330**, 113–139.

DEIGAARD, R. & FREDSØE, J. 1989 Shear stress distribution in dissipative water waves. *Coastal Engng*, **13**, 357–378.

DUNCAN, J. H. 1981 An experimental investigation of wave breaking produced by a towed hydrofoil. *Proc. R. Soc. Lond.* A **377**, 331–348.

HASSELMANN, K. 1971 On the mass and momentum transfer between short gravity waves and larger-scale motions. *J. Fluid Mech.* **50**, 609–638.

HENDERSON, F. M. 1966 *Open Channel Flow*. Macmillan.

HORNUNG, H. G., WILLERT, C. & TURNER, S. 1995 The flow field of a hydraulic jump. *J. Fluid Mech.* **287**, 299–316.

KIRBY, J. T., BAKUNIN, J. & HUQ, P. 1995 Turbulence measurements in low Froude number hydraulic jumps. *Proc. 10th ASCE Engng Mech. Conf.*

LIN, J. C. & ROCKWELL, D. 1995 Evolution of a quasi-steady breaking wave. *J. Fluid Mech.* **111**, 29–44.

LONG, D., STEFFLER, P. M. & RAJARATNAM, N. 1991 A numerical study of submerged hydraulic jumps. *J. Hydraul. Res.* **29**, 293–308.

McCORQUODALE, J. A. & KHALIFA, A. 1983 Internal flow in hydraulic jumps. *J. Hydraul. Engng ASCE*, **109**, 684–701.

MADSEN, P. A. & SVENDSEN, I. A. 1983 Turbulent bores and hydraulic jump. *J. Fluid Mech.* **129**, 1–25.

PEREGRINE, D. H. & SVENDSEN, I. A. 1978 Spilling breakers, bores and hydraulic jumps. *Proc. 16th ICCE*, 540–550.

QUINGCHAO, L. & DREWES, U. 1994 Turbulence characteristics in free and forced hydraulic jumps. *J. Hydraul. Res.* **32**, 877–898.

RESCH, F. J. & LEUTHEUSSER, H. J. 1972 Reynolds stress measurements in hydraulic jumps. *J. Hydraul. Res.* **10**, 409–430.

RESCH, F. J., LEUTHEUSSER, H. J. & COANTIC, M. 1976 Etude de la structure cinematique et dynamique du ressaut hydraulique. *J. Hydraul. Res.* **14**, 293–319.

ROUSE, H., SIAO, T. T. & NAGARATHNAM, S. 1959 Turbulence characteristics of the hydraulic jump. *Trans. ASCE*, **124**, 926–966.

SCHÄFFER, H. A., MADSEN, P. A. & DEIGAARD, R. 1993 A Boussinesq model for breaking waves in shallow water. *Coastal Engng* **20**, 185–202.

SVENDSEN, I. A. & MADSEN, P. A. 1984 A turbulent bore on a beach. *J. Fluid Mech.* **148**, 73–96.

SVENDSEN, I. A., MADSEN, P. A. & HANSEN, J. B. 1978 Wave characteristics in the surf zone. *Proc. 16 ICCE*, 520–539.

YEH, H. & MOK, K.-M. 1990 *On turbulence in bores. Phys. Fluids* A **2**, 821–828.

YEH, H. 1991 Vorticity generation mechanisms in bores. *Proc. R. Soc. Lond.* **432**, 215–231.